DESIGN AND FABRICATION OF MWCNT-PDMS COMPOSITE POLYMER-BASED FLOW SENSOR FOR LOW FLUID FLOW DETECTION

by

Rezoana Bente Arif

A Thesis Submitted in Partial Fulfillment of the Requirements for the Degree of Master of Engineering in Nanotechnology

Examination Committee:	Dr. Tanujjal Bora (Chairperson) Prof. Manukid Parnichkun Dr. Bhawat Traipattanakul
Nationality:	Bangladeshi
Previous Degree:	Bachelor of Science in Electrical, Electronic and Communication Engineering Bangladesh University of Professionals Bangladesh
Scholarship Donor:	Asian Development Bank–Japan Scholarship Program (ADB-JSP)

Asian Institute of Technology
School of Engineering and Technology
Thailand
May 2021

AUTHOR'S DECLARATION

I, Rezoana Bente Arif, declare that the research work carried out for this thesis was in accordance with the regulations of the Asian Institute of Technology. The work presented in it are my own and has been generated by me as the result of my own original research, and if external sources were used, such references have been cited. It is original and has not been submitted to any other institution to obtain another degree or qualification. This is a true copy of the thesis, including final revisions.

Date: 14.05.2021

Name: REZOANA BENTE ARIF

Signature:

ACKNOWLEDGMENTS

My first and foremost gratitude towards the almighty God for His blessings upon me. I would like to show my eternal gratefulness to my supervisor as well as the chairperson of my thesis Dr. Tanujjal Bora for his constant support, guideline, understanding and instruction with his profound knowledge. Moreover, I would like to show genuine thanks to the committee members Prof. Manukid Parnichkun and Dr. Bhawat Traipattanakul for their valuable comments as well as suggestions in order to improve my work. I am greatly indebted to ADB-JSP scholarship for giving me financial support throughout my study period at AIT. My most profound appreciation to all my friends of AIT who worked with me in the COEN laboratories. Their help in understanding the equipment from time to time made my path easier to complete the research. My special thanks to my mother and my husband for giving me mental support. Lastly, my love and respect for my late father, with whom I believe I am still connected somehow for his deep adoration to me.

ABSTRACT

Here, we report the fabrication of a liquid flow rate sensor using multi-walled carbon nanotube (MWCNT) reinforced conducting polydimethylsiloxane (PDMS) polymer. The polymer composite was prepared by mixing different amount of MWCNT into the PDMS matrix, where the electrical conductivity of the insulating PDMS was observed to improve with the increasing amount of MWCNT. At 10 wt.% MWCNT concentration, the PDMS film exhibited an electrical resistance of 4.17 kΩ, which was further reduced to 2.55 kΩ by increasing the MWCNT concentration to 12 wt.%. The as-prepared MWCNT-PDMS films showed good mechanical strength and flexibility. Using the 12% MWCNT-PDMS nanocomposite films, a sensor to detect the flow rate of a liquid through a channel was developed. The designed sensor system showed a good response against different flow rates of water, where the film resistance was observed to increase with increasing flow rate due to the bending exerted on the film by the liquid flow. With the sensor designed in this study, a limit of detection (LOD) of 150 µl/s was achieved, which is comparable to many of the commercially available sensors. The MWCNT-PDMS flow rate sensor presented in this study has the potential to detect low flow rates in the µl/s range, which can be beneficial for biomedical applications. Besides the effectual measurement of the low flow rates of liquid, the sensor is inexpensive and very easy to fabricate.

CONTENTS

LIST OF TABLES

LIST OF FIGURES

LIST OF ABBREVIATIONS

CFPLA = Carbon Fiber PLA
CNT = Carbon Nano Tubes
CVD = Chemical Vapor Deposition
DCM = Dichloromethane
EMF = Electromotive Force
EVAR = Endovascular Aneurysm Repair
FBAR = Film Bulk Acoustic Resonator
FP = Fabry–P´erot
IPA = Isopropyl Alcohol
IR = Infrared Radiation
LOC = Lab-On-Chip
LOD = Limit of Detection
MEMS = Micro Electro-Mechanical System
MWCNT = Multiwalled Carbon Nanotube
OSTE = Off- stoichiometry thiol-ene
PIV = Particle Image Velocimetry
PD = Positive Displacement
PDMS = Polydimethylsiloxane
PLA = Polylactic Acid
PMMA = Polymethyl Methacrylate
SAW = Surface Acoustic waves
SEM = Scanning Electron Microscopy
SNR = Signal-to-Noise Ratio
SO = Silicon Oil

CHAPTER 1
INTRODUCTION

1.1 Background of the Study

Today nanomaterials are widely being used in various fields of bio and nano sensing applications. For example, they are useful for the sensation of multiple aspects of the heart, respiratory system, blood (Zhou, Wang, & Cui, 2015), detection of food contaminants (Eivazzadeh-Keihan, Pashazadeh, Hejazi, de la Guardia, & Mokhtarzadeh, 2017; Baek et al., 2020), to agriculture usage (Prasad, Kumar, & Kumar, 2017) and to monitoring and cleaning of the environmental pollution. Due to their small sizes, nanosensors are popular and getting demands in the control system in automation, environmental revival, micro-biological treatment, bio-medical defense and electronic chip miniaturization and versatility in chip performance and so on. The performance of these devices highly depends on the flow rates of the fluid. Therefore, monitoring the low flow and controlling them is essential to ensure the proper functioning of such devices.

In recent years, a considerable number of researches have been conducted in the field of microfluidic and microchannel devices, and research related to the flow rate monitoring in these devices are, therefore, also gaining momentum. With the keywords “low flow rate” and “sensor”, a total of 4,906 publications were found in Science Direct in the last 20 years, which show a gradual and exponential rise in the number of publications over time. However, this number is order low if we search for the keyword “microfluidic” in Science Direct, which returned a value of 47,048 publications for the same period. The trend clearly shows that there is an increasing interest in research for the development of low flow rate sensors. However, the design of these low liquid flow rate sensors with less complexity and their cost is still challenging and needs more attention to make them industrially viable.

Figure 1.1

An Overview of Increase in the Number of Publications on Microfluidic and Low Flow Sensors

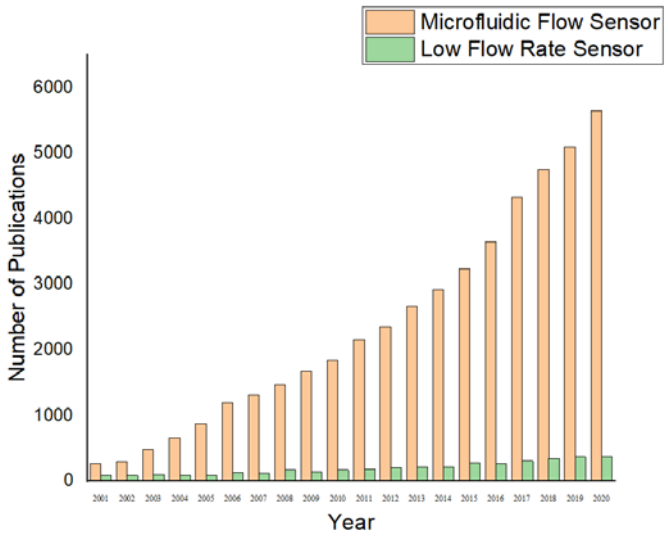

1.2 Statement of the Problem

In the last 20 years, due to the boost in microelectronics, micro devices, such as micro-pump, micro motor etc., the microfluidic control in those devices is turning into a demanding issue. Because of the device size having extremely small, the operating variables monitoring and controlling the performance of these micro devices with high precision is a matter of concern. However, with the period of time gradually, the number of researches on improving the accuracy of their performance is progressing. There are manifold approaches for low fluidic flow sensation. The low flow rate of liquid can be measured by using different methods and properties (Mark, Haeberle, Roth, Von Stetten, & Zengerle, 2010); such as the mechanical displacement due to the liquid flow, the lateral flow of liquid through porous medium, pressure gradient, electric field gradient, surface wave analysis of liquid droplet and so on.

However, to design a low liquid flow sensing device, the main concerns are basically its short response for sensing, portability, precise sensitivity, industrialization and low cost. In spite of the exponential rise in the research in the low liquid flow sensor, most of them are failing to fulfil the criteria of industrialization of the product because of the complex manufacturing process, expensive mass production process. While preparing the multiwalled carbon nanotube (MWCNT) composite PDMS polymer, a

homogeneous distribution of the composite is required, but the powder form of MWCNT may impair the equal distribution. These are the very specific challenges that should be taken under consideration while fabricating and characterizing the pressure sensor for the low fluidic flow rate to have prominent outcomes.

On top of that, the diverse fabrication processes of the low-fluidic sensor are comparatively cheap and very easy working principle; there is a restriction in polymer selection while fabrication. An only flexible type of polymers should be used in their fabrication process. Very commonly used polymer in microfluidic sensors is PDMS (Polydimethylsiloxane) due to their flexibility, optical transparency and capability of real-time performance (Martin & Bhushan, 2017), Poly ethylene terephthalate for flexibility, inert behaviour and adversity to moisture (Fallahi, Zhang, Phan, & Nguyen, 2019), Off- stoichiometry thiol-ene (OSTE) (Juhong Chen et al., 2015) for flexibility under UV environment and so on. In addition, in some cases, for mechanical feasibility, the strength of the material for making it a handful is required. For this purpose, composite polymer preparation is necessary, which might be a complex process.

1.3 Objectives of the Study

Predominantly the purpose of this thesis is to develop a pressure sensing system based on flexible electrically conductive polymer which will be capable of measuring the low flow rate of liquids. For this motive, the specific objectives are mentioned below:

1. To develop an MWCNT-PDMS composite polymer film and make it electrically conductive.
2. To evaluate the electromechanical characteristics of the MWCNT-PDMS at different bending angle conditions.
3. To fabricate a flow sensor using this composite film to detect liquid flow rates in µl/s scale.

1.4 Scope

The scope of this thesis is within the field of measurement of the low flow rate of non-conductive liquid in biomedical devices. The elementary materials used to develop the liquid flow rate sensor are MWCNT and PDMS based composite polymer. The change in its electrical resistance due to the applied pressure on the composite film will be

utilized to sense the liquid flow rate. To construct some parts of the sensor assembly, 3D printing technology will be used.

1.5 Limitations

1. The sensor material is limited only to the MWCNT filled PDMS polymer composite. No other sorts of CNT or polymer, or other composites were used, and the weight percentage of MWCNT was limited to 12%.
2. No other polymer rather than PDMS polymer will be used.
3. The analysis of the flow rate detection will not be performed for different types of liquids. Rather this study will be confined to only distilled or deionized water.

1.6 Organization of the Study

This dissertation is divided into five chapters which are schemed as follows:

Chapter 1 is composed of the background of the study, statement of the problem, objectives, scopes, limitations and the organization of the study.

Chapter 2 describes the literature review regarding different flow meters, their conveniences, limitations and applications; usage of MWCNT-PDMS sensors.

Chapter 3 presents the methodology of the processes required to develop and characterize the sensor designed in this research.

Chapter 4 deals with the results regarding the fabrication and characterization of the MWCNT-PDMS film, system behaviour and flow measurement.

Chapter 5 demonstrates the summary of the study with the conclusion, application, limitations, future works of this study.

CHAPTER 2
LITERATURE REVIEW

Flow sensors have been being a certain device in the fluid mechanic systems while it has been a desiring term in the field of microfluidic flow assessment. Following the basic principles of manifold flow meter technology, mini flow sensors are now being developed to measure the fluid profile of low flow rate. For this purpose, it is most obvious to integrate thermal, electro-chemical or electro-mechanical process altogether to analyze the small flow rate. The main reasons for the rise in their demand are the control system in automation, environmental revival, micro-biological treatment, bio-medical defence and electronic chip miniaturization and versatility in chip performance and so on.

Several types of microfluidic flow sensors exist to measure the flow features for stratified flow or unstratified flow. Some are on the basis of the thermal process, and some are based on mechanical pressure deflection, where others work following the electro-mechanical, electro-chemical and optical principles. These micro sensors have been produced by means of different Silicon wafer technologies (Micro-Electro-Mechanical System) MEMS-based technologies (Whitesides, 2006) with the variation of chemical elements and their different fabrication process (etching, lithography, chemical deposition method etc. Meanwhile, the basic concept of all these microfluidic sensors is to convert any natural signal to any required electrical signal mostly (Antony, Nandagopal, Sreekumar, & Selvaraju, 2014).

In this chapter, an overview of the working mechanism, various micro fabrication process and applications, as well as limitations of manifold low flow sensor technology are discussed. Microfluidic flow sensors are dependent on different mechanisms, such as thermal, mechanical, electromagnetic, optical as well as electromagnetic principles. Depending on the design parameters, flow sensing mechanism, fluid types, cost, sensitivity, the sensor can be utilized for various purposes in low fluid flow analysis and measurement. Mostly, the low flow sensors are beneficial in lab-on-chip and biomedical applications. In Figure 2.1, an overview of various type of flow sensors for low flow rate analysis is exhibited.

Figure 2.1

Different Types of Flow Sensors

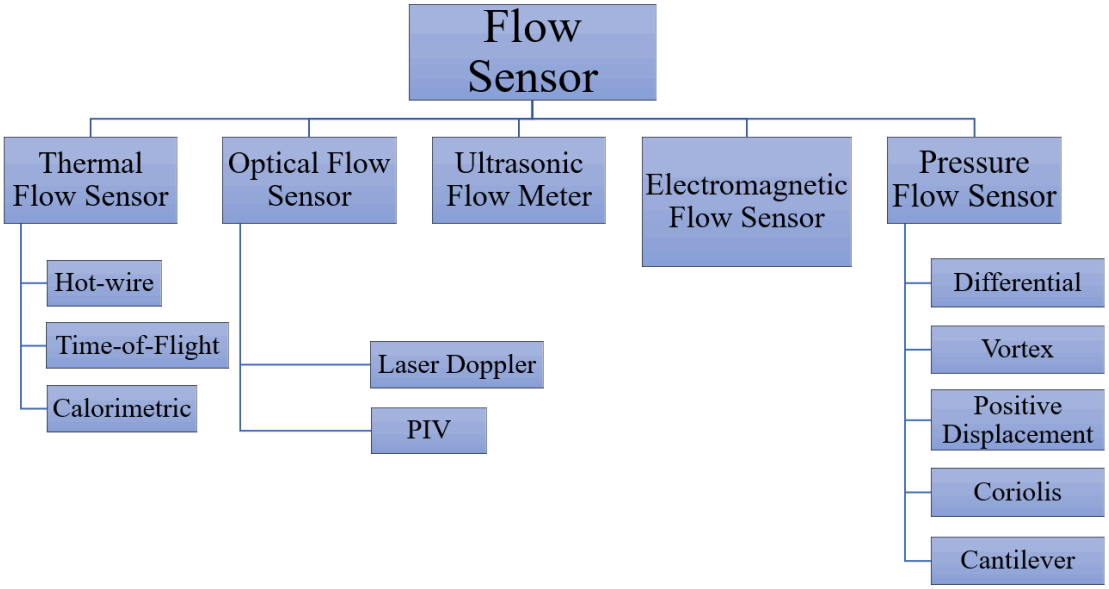

2.1 Thermal Flow Meter

The basic principle of thermal flow meters is to sense the flow profiles using the heat or temperature difference of linear property. The preliminary shortcomings of the thermal mass flow meters are: (a) sensitivity toward bubble (b) non-linear behaviour (c) mostly gas applications (Chung 2019). Nevertheless, gradually by overcoming the limitations, they are becoming desirable in microfluidic analysis in biomedical perspectives due to their improvised high sensitivity and accuracy (Davaji 2016).

2.1.1 Hot Wire Flow Meter

Mechanism For mass volumetric flow measurement or microfluidic flow rate determination, hot wire-based or hot film-based thermal flow meters are basically used respectively either in constant resistance or Constance temperature mood. A Wheatstone bridge model is collaborated with ***a*** microfluidic system to determine the flow rate through a microchannel (Kuo, Chang et al. 2011). A film sensor or tungsten placed through the path of the fluid flow is connected as a resistive load of the bridge. This film is subjected to be heated initially and continuously even after. Initially, the bridge is kept resistively balanced phase (i=0, R_1 /R_2=R_3/R_4). As the fluid temperature**,** in the beginning, is less than the temperature of the film or tungsten filament in Figure 2.2, the fluid absorbs the heat from the film while flowing through the channel

according to the heat transfer method. In such a case, the resistance of the film or the tungsten wire gradually gets changed due to the temperature effect on it as well as the galvanometer starts to show some value of current. For the purpose of keeping this system in a null position, a continuous supply of heat is provided to the filament and keep the temperature difference between the filament and the fluid a constant (King 1914). In some cases, two filaments of different temperature are used, and their temperature difference is taken under consideration in replacement of fluid- filament temperature difference. From the temperature difference, the flow rate is identified. As the current flow through the bridge is maintained on a constant value, it is considered to be a constant current method. The governing Equation can be converted into energy to characterize the flow rate, channel dimensions and pressure effects (Siddiqui, Haroon et al. 2013). On the other side, in the constant temperature method, the bridge is kept in a null position instead of flow through the channel, as well as the change in resistance using the rheostat. This variable resistance is kept on adjusting the bridge resistance while imbalance occurs due to the flow. Normally, the hot wire is used in case of large flow measurement while hot-film is feasible to determine the small amount of flow or micro and nano-level flow.

Figure 2.2

Basic Schematic of Hot-Wire or Hot-Film Flow Sensor

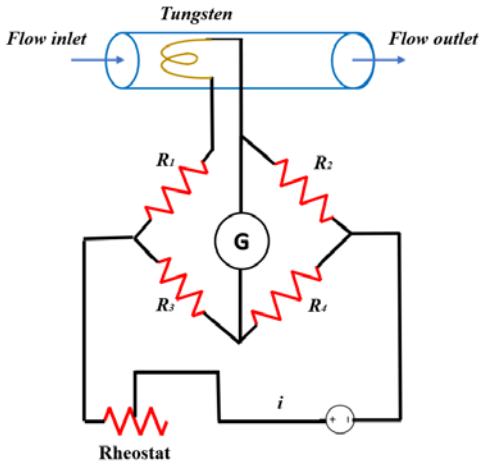

Advantages and Limitations Besides a long-term use of hot-wire flow sensor in mass flow assessment, they have been treated popular enough in the microfluidic flow analysis for low-velocity calibration (Grandchamp, Van Hirtum et al. 2010) and also

high sensitivity in microfluidic flow measurement (Li, Yan et al. 2015). Although hot-film can execute better performance in spatial resonance in terms of heat transmission on the surface than some other flow metering system, the frequency response limit may affect the measurement (O'Donovan, Persoons et al. 2011). Moreover, hot-film sensors require a continuous calibration for the temperature or resistance balance; however, different calibration method such as neural network hot-film calibration can provide sustainable usage (Kit and Liberzon 2016) and also the selection of film material has a limitation in terms of their thermal conductivity coefficient (Kuo, Yu et al. 2012).

2.1.1.1 **Applications** This Hot-wire thermal flow sensor can be used in biochemical applications due to its high sensitivity and broad dynamic extent (Li, Yan et al. 2015). Kuo, Jonathan TW, et al. demonstrated that a very low flow rate of retinal fluid through a porous channel could be achieved using a hot-film flow meter either by means of constant temperature or constant current method (Kuo, Chang et al. 2011).

2.1.2 Time-of-Flight Flow Sensor

2.1.2.1 **Mechanism** In a typical time-of-flight flow sensor, there are a minimum of one heater on the upstream side and one sensor part on the downstream side of the flow. This sensor measures the flow rate on the basis of the time difference of the flow of generated heat from the heater to the sensor (Chung 2019). The heater, thermally detached from the layer. In Figure 2.3(a), a time-of-flight flow-meter with one heater and one sensor is demonstrated, where Figure 2.3(b) shows one heater on the upstream side and two sensors on the downstream side. The time-lapse of the temperature imparity is measured as well as the flow rate of the fluid from the Eq. 2.1-2.4 (Van Kuijk, Lammerink et al. 1995):

$$T\left(l,\tau\right)=\frac{q}{4\pi k\tau}e^{-\frac{(l-v\tau)^2}{4\alpha\tau}} \quad \text{..... (Eq. 2.1)}$$

Where T is the temperature imparity for τ time-lapse; l is the gap between the heater and the sensing body; q is the pulse signal input strength; k is the thermal conductivity of fluid; α is the thermal diffusivity.

The two possibilities from the above Eq. are:

$$\tau_1=\frac{-2\alpha+\sqrt{4\alpha^2+v^2d^2}}{v^2};if,v\neq 0 \quad \text{..... (Eq. 2.2)}$$

$$\tau_2=\frac{d^2}{4\alpha};if,v=0 \quad \text{..... (Eq. 2.3)}$$

And the average flow velocity,

$$v = \frac{d}{\tau} \ldots\ldots\ldots\ldots \text{(Eq. 2.4)}$$

Figure 2.3

(a) A Very Basic Schematic of Time-of-Flight Flow Sensor (Kuo, Yu et al. 2012) (b) Time-of-Flight Measurement Method (Chung 2019)

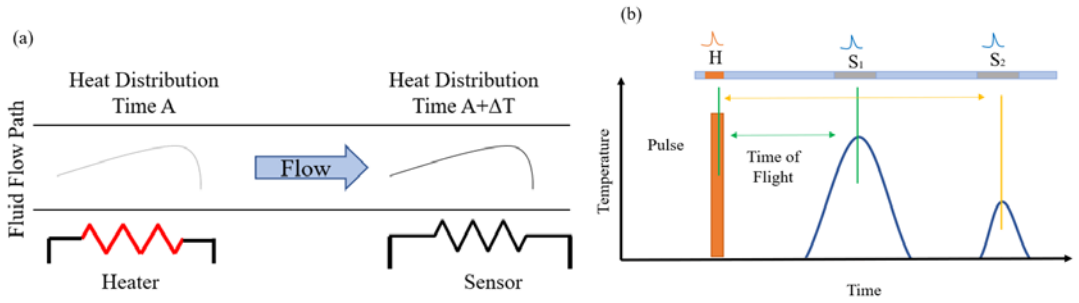

2.1.2.2 **Benefits and Limitations** Among the three types of thermal microfluidic flow meters, time-to-flight microfluidic sensor are independent on the types of fluid and illustrates linearity in their performance for lab-on-chip uses. Time-to-flight thermal sensor along with non-magnetic resonance showed a great benefit over optical technique in terms of noninvasiveness in the assay done by Harel, Elad et al. Because, with the absence of the tracer in the system, it is possible to find the flow rate of various species fluid, however, a compatible geometric is required to trace and monitor the chemical reaction (Harel, Hilty et al. 2007). They have more longevity and low power consumption than the other types of the thermal flow meter. Besides, normal thermal flowmeters have shortcomings; e.g. (a) corrosion as well as the reduced lifespan of the heater and sensor (b) disturbance to the fluid flow because of the heater and sensor in their flow path (c) Huge power requirement for the thermal conversion process etc. in mass flow measurement. But thermal flow meter can provide a gravity-controlled accurate mass flow meter with a proper calibrate system (Chung 2019).

2.1.2.3 **Applications** This sort of flow sensor has been being used to analyze microfluidic velocity profile in a lab-on-chip (Berthet, Jundt et al. 2011). In biomedical application, besides other thermal sensors, the time-of-flight microfluidic flow-meter contributes prominently. Time-of-flight flow sensors are capable of analyzing imbalanced material in bio fluid (Chen, Li et al. 2019), cytometric analysis (Bandura,

Baranov et al. 2009), as well as coronary blood, flow analysis in positron emission tomography (PET) (Suda, Onoguchi et al. 2016) and many more. Therefore, it is quite visible that this type of flow sensor is notable in the microfluidic analysis.

2.1.3 Calorimetric Flow Sensor

2.1.3.1 **Basic Principle** Alike the time-of-flight sensor, the calorimetric flow sensor is comprised of heater and sensor through, here, at least two sensors are placed on the two sides of the heater. Initially, the flow temperature is sensed by the first sensor on the upstream side; then, sensor number 2 senses the temperature of the heated fluid after passing through the path of the heater. This temperature distribution throughout the flow time delay is used to measure the flow rate of the fluid with the help of Eq. 2.5 (Van Kuijk, Lammerink et al. 1995):

The temperature variation between sensor one and sensor 2 is:

$$\Delta T = T_H\left(e^{\beta_1 l_1} - e^{\beta_2 l_2}\right) \ldots\ldots\ldots\ldots \text{ (Eq. 2.5)}$$

Here, l_1 and l_2 are the distance of sensor 1 (upstream) and sensor 2 (downstream) from the heater, respectively and $\beta_{12} = \dfrac{v \pm \sqrt{\left(v^2 + 16b^2k/\delta^2\right)}}{4bk}$.

Figure 2.4

Schematic of a Basic Calorimetric Flow-Meter Mechanism (Kuo, Yu, & Meng, 2012)

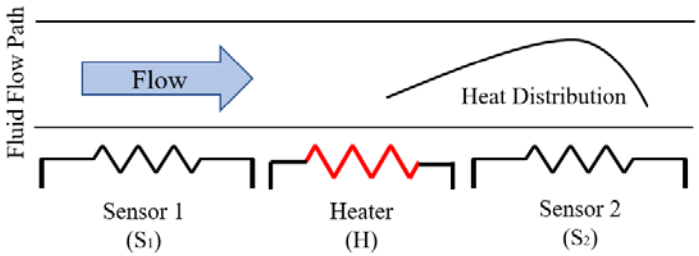

2.1.3.2 **Advantages and Applications** Since the calorimetric flow-meter consists of two sensors in symmetric position with respect to the heater, they are capable of analyzing flow in both directions. Calorimetric microfluidic flow sensors are compatible for measuring microfluidic flow in the respiratory system and other biomedical applications because of their comparatively low power consumption than other thermal flow sensors (Kitsos, Demosthenous et al. 2019). Furthermore, recently several assays illustrated that they also could sense the flow profile of low flow fluid of

micro or nano range precisely (Davaji, Jeong Bak et al. 2014, Baldwin, Hudson et al. 2018).

2.2 Optical Microfluidic Flow Meter

2.2.1 Laser Doppler Flow Meter

Mostly alike the ultrasonic flow meter, the Laser Doppler Flow meter is operated under the Doppler effect of the optical wave. Here, two laser beams of the same wavelengths are incident on the fluid channel at a specific point of desire from a cross position. The interference between the beams produces diffracting beam perpendicular to the flow through the channel. Depending on the cross intersectional angle (θ) between the beams and their wavelength (λ), the fringe spacing, as well as the velocity of the fluid, can be measured.

$$d = \frac{\lambda}{2\sin(\theta/2)} \quad \text{..... (Eq. 2.6)}$$

$$\nu = \frac{f\lambda}{2\sin(\theta/2)} \quad \text{..... (Eq. 2.7)}$$

where f is the new frequency extracted from Fourier transformation. For a various number of particles flowing through the channel, the position and spacing of the fringes varies (Rubenstein, Yin et al. 2015). From the scattering fringes, the position of the particle in the flow can be found within a specific time. Finally, this time is divided by the distance and thus get the velocity of the fluid.

2.2.2 PIV Flow Meter

Particle Image velocimetry is a highly favoured and desired technique to measure the microparticle position and microfluidic velocity profile in laboratories. In this process, one or mostly more cameras are set at a different angle with the channel. And when fluid or particle with a different refractive index rather than the channel medium refractive index flow through it, it creates refractive patterns. These multiple patterns are captured by the cameras, which are later compiled in software to get the distance of the fluid at a particular time. Eventually, the velocity of the fluid is calculated from a distance covered by the particles and the duration to pass the distance (Rubenstein, Yin et al. 2015).

Figure 2.5

Basic Diagram of (a) Laser Doppler (b) PIV Flow Meter (Rubenstein, Yin et al. 2015)

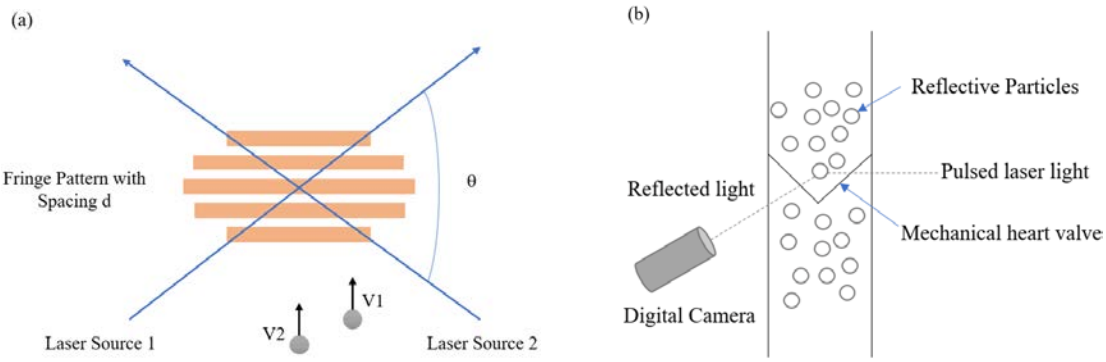

2.2.3 Benefits and Limitations

Optical biosensor based microfluidic flow meters shows nanomolar sensitivity and very specific in time while dealing with the low cytometric flow (Chen, Schoeler et al. 2018). On top of that, optical flow meters are able to detect the flow rate directly and invasively (Lima, Wada et al. 2007), and optical Doppler microfluidic flow meter with depth resolution is beneficial in optic flow detection (Leitgeb, Werkmeister et al. 2014). However, in some PIV produced three-particle images affects the size of the sensor (Angarita-Jaimes, McGhee et al. 2006) where some PIV systems require sophisticated systems and complicated calibration to avoid error and to ensure better accuracy (Cierpka and Kähler 2012). These phenomena arise complexity in the system for the reason why it is tough to make use in mass production. Although PIV provides a parabolic velocity profile throughout the microchannel, some fluctuation may appear simultaneously (Lima, Wada et al. 2007).

2.2.4 Applications

Among a huge number of applications of optical low flow meter in bio-medical area and biomedicine, PIV is used for the analysis of the dynamics of a protein in cells (Travagliati, Girardo et al. 2013). Recently, Hallam, Rigas et al. came up with an approach of Optical Coherence Tomography with a single entry of optical source only to measure micro-level flow (Hallam, Rigas et al. 2020). Besides, PIV is highly used and convenient for lab research as well as miscellaneous Lab-on-CD tests (Silva, Semiao et al. 2019). PIV flow sensors require highly sensitive external devices to get operated.

2.3 Ultrasonic Flow Meter

2.3.1 Basic Mechanism

In mostly used single path ultrasonic flow meters, two transducers as sensors are installed in a cross angled position on the pipe surface, around in a 45^o or 30^o or basically less than 90^o angle. They are treated as transmitter and receiver both since both transmit and receive signals from each other in 'W' or 'Z' or 'V' shaped path (Zhang, Guo et al. 2019). Figure 2.6 (a) exhibits that the transducer A and B are placed in an angular position less than 90^o (θ). When there is no flow through the channel, the transient time propagation for A to B (t_1) and B to A (t_2) of a signal is zero, with either be treated as transmittance and acceptance. However, while a fluid with velocity V flows through a channel of L length and D diameter, it realizes an acoustic velocity (C). The transducer uses the transient time difference to convert the signal to an electrical signal resulting in the flow rate of the fluid in it. For this purpose, Eq. 2.8 and 2.9 can be applied where α and β are the circuit time delays for transducer A and B, respectively.

$$t_1 = \frac{L}{C + \cos\theta} \quad \text{..... (Eq. 2.8)}$$

$$t_2 = \frac{L}{C - \cos\theta} \quad \text{..... (Eq. 2.9)}$$

Average Velocity (V_{avg}) can be derived from the transient time difference, which is,

$$v_{avg} = \frac{L}{2\cos\theta}\left(\frac{1}{t_1 - \alpha} - \frac{1}{t_2 - \beta}\right) \quad \text{..... (Eq. 2.10)}$$

Figure 2.6

(a) Basic Structure and Mechanism (b) Cross Section of Ultrasonic Flow Meter (Guo, Sun et al. 2014)

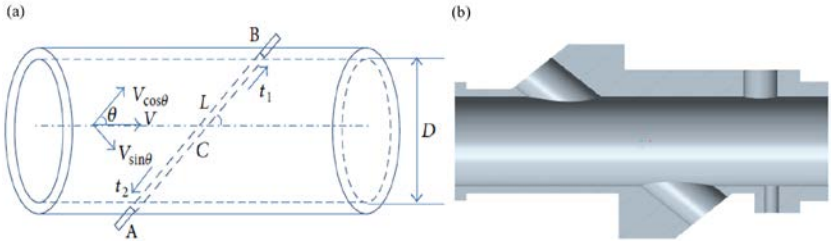

Though it is considered to have a uniform flowrate throughout the channel, practically there is change in profile of the flow in different points of the channel due to the viscosity, installation process, transient time measuring process, ambient condition, flow meter uncertainty etc. (Zhang, Guo et al. 2019 and Hogendoorn, Hofstede et al. 2011). Therefore, the average value of the flow velocity is taken under consideration finally. Another sort of ultrasonic sensors is operated essentially based on the Doppler effect in which the frequency shift is measured in between the transmitter, receiver and the carrier of the fluid. There is a wave difference between the wave from a sound source and when there is a flow for which the position of the source is changed. And thus, converted to flow rate using piezoelectric devices or transducer (Stern, Bakal et al. 2014).

2.3.2 Microfluidic Ultrasonic Flow Meter

Ultrasonic or acoustic sensors have been being pretty much a neoteric application and research in the case of microfluidic flow mixing and their transportation. Microfluidic ultrasonic flow sensor consists of two basic parts corresponds to (a) active parts: micropumps like devices and (b) microchamber like segments. On the other side, for the reason of the high cost and complexity of micromechanical pumps, recently they are replaced with non-movable micropump structures, which works based on electro-kinetic or surface related forces (Luo, Fu et al. 2013). Owing to the upgrading demands in biomedical, lab-on-chip (LOC), nano-sensing etc., the structures as well as the orientation of material and instruments in the micro ultrasonic sensors are being shifted to more efficacious patterns.

2.3.3 Advantages and Limitations

In comparison with the other types of microfluidic flow meter, acoustic flow sensors are more compatible in terms of making LOC a compact and highly responsive sensing device. Although SAW (Surface Acoustic Waves) sensors are beneficial in terms of small size, sensitivity, collaboration with Silicon electronics, they lack strong signal and higher quality factor (Luo, Fu et al. 2013). Through this type of flow-meter are quick responsive in low flow measurement, the low accuracy in their performance is yet a demerit (Schena, Massaroni et al. 2015).

2.3.4 Applications

The positive features of various form of the ultrasonic or acoustic sensor have been making the industrial, biomedical and analytical sector highly enthusiastic about them. They are essentially able to detect pH level, viscosity, velocity, conductive, radiation and electric properties, fluid mixing process and fluid transporting process. Besides, acoustic sensors are very popular in bio-medical sensing: blood cell analysis and enumeration (Gnyawali, Strohm et al. 2019) and also surface wave acoustic microfluidic sensors are beneficial in the analysis of microfluidic bio-sample (Luo, Fu et al. 2013).

2.4 Electromagnetic Flow Meter

2.4.1 Working Principle

Based on Faraday's Law of Electromagnetic induction, an electromagnetic flow meter can be operated, and the conductive fluid flow rate can be traced. According to Faraday's law, if any conductive or current-carrying matter is placed inside a magnetic field, the matter will be induced by an electromotive force (emf). Based on this phenomenon, the non-conductive flow channel is placed inside a magnetic field with electrodes. When conductive fluid flows through the pipeline, an emf (E) is produced, which is proportional to the fluid density (B), length of the fluid flow (distance between the electrodes) (l) and the velocity of the fluid (v). In Eq. (2.11), the fluid density is fixed for any particular fluid, and the channel length is also constant. Therefore, the induced emf is directly proportional to the fluid velocity, and so the velocity of a flow rate of the fluid can the recorded from the electrodes (Shercliff 1962). There have been manifold electromagnetic flow meters developed for open channel large flow (Watral, Jakubowski et al. 2015); however, the number in case of low flow measurement using this method is comparatively less.

$E \propto Blv$ …… (Eq. 2.11)

There is diversity in the fabrication and assembly of electromagnetic flow sensor in the case of microchannel devices. For example, *Mi, Shengli, et al.* proposed a process for cell analysis and fluid flow on an organ chip with a mini electromagnetic pump. The system of PDMS (Poly-di-Methyl Siloxane) and PMMA (Polymethyl Methacrylate) coil membrane and Nd-Fe-B magnet was assembled with the bonding of oxygen plasma (Mi, Pu et al. 2020). Another example of a cost-effective and easy-to-design

electromagnetically operated valve to control microfluidic flow was developed with series of Solenoid and PDMS (Pradeep, Stanley et al. 2018).

Figure 2.7

Schematics of Electromagnetic Flow Meter (Watral, Jakubowski et al. 2015)

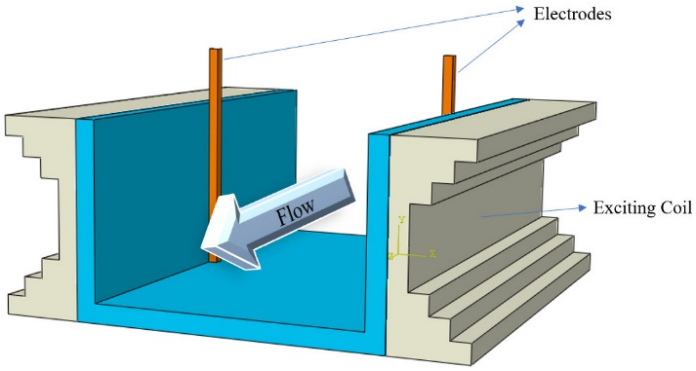

2.4.2 Benefits and Limitations

The major cause of its being so popular is the simplicity in the structure, and moreover, the construction bodies are completely fixed. Also, due to not containing any rotating or moving body, there is no sensitivity issue in mechanical bearing or pressure loss. They are cost-effective with high accuracy performance. On the other hand, mostly the only limitation with this type of flow meter is to be capable of measuring the flow rate only the conductive fluid (Smart Measurement, 2020), and in of the microfluidic flow, sometimes it shows diversity in their performance. Recently, various assays are going on to improve the accuracy in their throughput for low flow measurements (Rustambekovich, Abdujalilovich et al. 2019).

2.4.3 Applications

To fulfil the necessity of the sensors in the bio-medical multi-disciplinary analyses, the demand for microfluidic flow meter is dramatically exaggerating in recent time. Because of the simple and required sensitivity in the case of microfluidic flow, electromagnetic flow detectors, also notable as ‘mag meter’, are now taken under consideration. Thus, lots of assays are performed and got successful for laboratory attempts. For example, electromagnetic based microfluidic sensors are highly stable for analyzing very low flow rate of fluid in biomedical, energy or lab-on-chip (Zarifi,

Sadabadi et al. 2018). Among other implication in the bio-medical field, electromagnetic flow sensors combining electrochemical methods are used to analyze cancer cell exosome (Jeong, Park et al. 2016).

2.5 Differential Pressure Sensor

2.5.1 Basic Principle of Differential Pressure Sensor

The very basic precept of Differential Pressure Sensor is to perform fluid detection, its presence, rate of flow and its type depending on the 'Bernoulli's laws' of Fluid mechanics (Wang, Chen et al. 2009). With the varying flow rate: means changed velocity, a dissimilar diameter of the fluid channel; the distinction in the pressure is observed; by means of which the fluid characteristics are studied. Bernoulli's law states that:

$$p + \rho g h + \frac{1}{2}\rho v^2 = k \quad \ldots\ldots\ldots\ldots \text{ (Eq. 2.12)}$$

Here, P is the pressure, ρ is the density of the fluid, g is the acceleration of gravity (9.8 ms^{-2}), v is the velocity of the fluid, h is the height of any point from a reference and k is a constant.

Figure 2.8

Pressure Variation Due to the Difference in Height (From Reference) and Diameter of the Channel

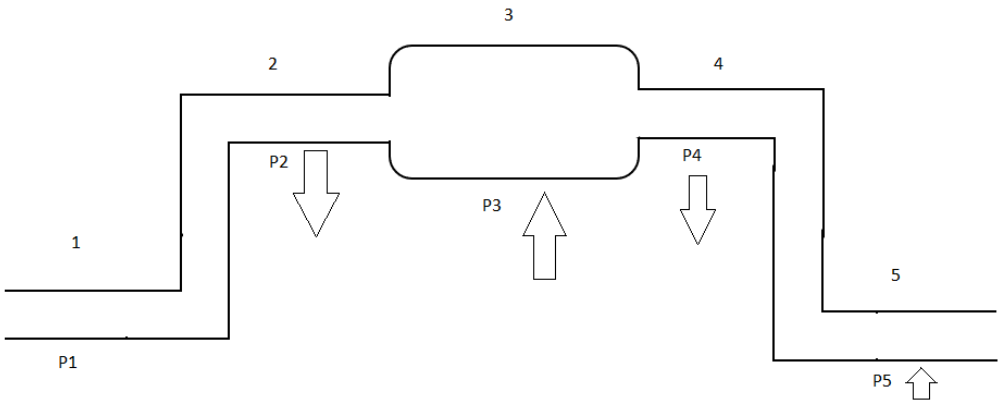

2.5.2 Various Forms of Different Pressure Sensors and their Mechanism

The height and velocity of the fluid are related inversely with the pressure inside the channel whereas, the area as well as the diameter of the channel is directly proportional to the pressure in it. Simply fabricated with P-type poly-Silicon and oxide layer deposition alternatively and afterward assembling with singulate cap, surface micromachined pressure sensor can be prepared to sense some phenomena of fluid flow. It was demonstrated precisely that in this differential pressure sensor for 0.01 ml/hr to 100 ml/hr flow rate of fluid, the pressure increases with the increase in flow rate. Besides, flow direction and viscosity can be detected perfectly with the sensor (Shakir, Srihari et al. 2008). Another approach to equip a differential pressure sensor is based on FBG (Fiber Brag Grating) with magnetic transfer. By means of FBG; though hard to fit in a sensor; can used to design a differential pressure sensing device without contacting directly with fluid. With a fixed magnet A and two movable magnets B, C, among which B is connected to an elastic corrugate diaphragm via a rigid line and C is linked with the FBG. When different pressures are given as input to the diaphragm, it moves resulting the magnet B moving up and down as well as FBG sensing the pressure change via C magnet.

Figure 2.9

(a) Schematic of FBG Based Differential Pressure Sensor (b) Sensing Unit of the Magnets (Lyu, Che et al. 2017)

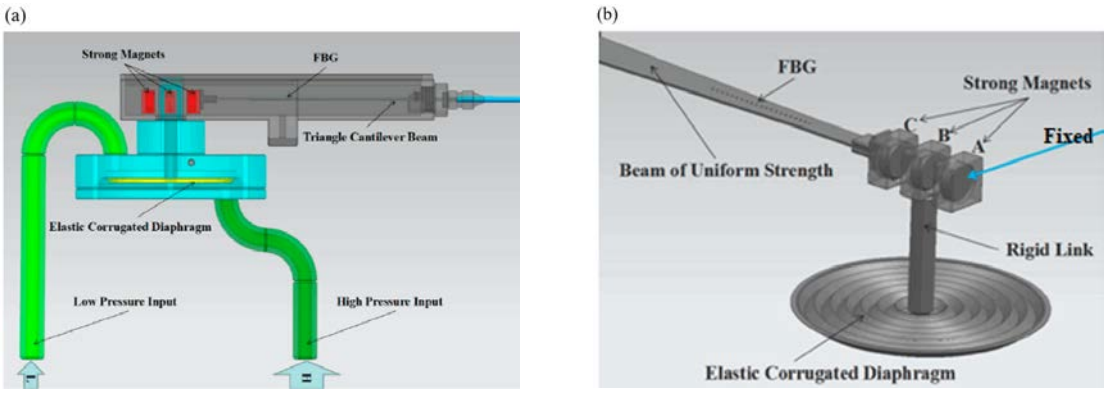

Using this type of differential sensor, the pressure within the range of 0kPa to 10kPa can be sensed with a sensitivity of 0.0112nm/kPa (Lyu, Che et al. 2017). Lee, Hyewon, *et al.* illustrated that by suspension of fluorescent particles, pressure detection is

precisely measured (Chung, Lee et al. 2009) where Orth, Antony *et al.* demonstrated that by varying the focal length of the pneumatic lens, pressure is changed and by means of this optical phenomenon pressure can be detected (Orth, Schonbrun et al. 2011). Both of these mentioned pressure sensors can be utilized in microfluidic devices. Therefore, it is shown that optical characteristic based differential pressure sensors are available in the literature though their mechanisms are different. Moreover, a device forming with luminescent in an air-filled channel was used to discern the pressure from 9 mbar to 5 bar with high sensitivity as well as the detection of temperature and oxygen in parallel. The advanced criteria of this type of sensor are that it was the very first microfluidic pressure sensor with a luminescent sensing layer inside the channel which can work with high sensitivity (Hoera, Kiontke et al. 2018). Keeping pace with the developed silicon industry, differential pressure sensors were developed using SOI (Silicon-on-Insulator) coupling with GOS (Glass-on-Silicon) by their pressure sensing bodies. Performing the finite element analysis on a modal interface and the sensitivity of the two resonators, a higher Q value was demonstrated, and it had hardly any impact on the resonators, which provided a precise environment to detect differential pressure (Li, Lu et al. 2020) From the above literature, it is shown that differential pressure sensors were developed with various mechanisms with the course of time.

Figure 2.10

Diagram of the Layers of a Differential Pressure Sensor (Li, Lu et al. 2020)

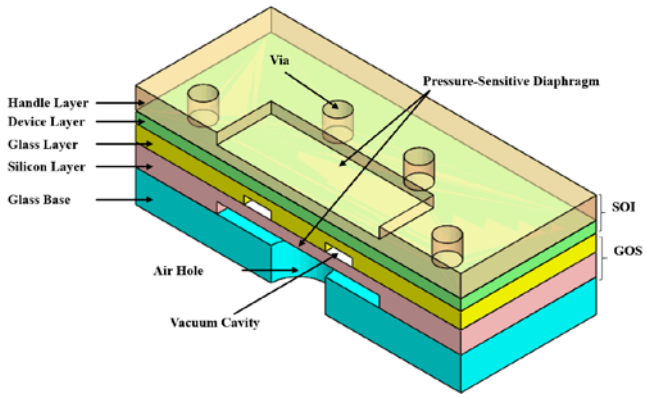

2.5.3 Advantages and Limitations

Sensing techniques that are operated with the mechanism of pressure difference have been providing a startling improvement in sensor technology. From the very beginning,

the manufacturing processes of these sort of sensors have been quite simple compared to other sensors. Moreover, day by day, they are more encapsulated for the microfluidic system with a higher sensing range and simpler analysis. Besides the flow rate analysis, they are now being utilized to determine the viscosity, presence of fluid as well as permittivity; which leads to fluid detection (Shakir, Srihari et al. 2008, Chung, Lee et al. 2009, Orth, Schonbrun et al. 2011). In the case of some differential pressure sensor, 100 times better performance was found compared to the static pressure sensors and also minimized the loss of energy which overpassed the performance of this type of sensors in the literature. On top of that, some are prominent for high temperature and overload conditions (Lyu, Che et al. 2017, Li, Lu et al. 2020). However, further researches, as well as developments, are yet to be performed to achieve their precise performance under extremely low flow rate, low pressure. Again, mass fabrications and industrialization with affordable cost are also required to be implemented.

2.6 Vortex Fluidic Flow Meter

2.6.1 Basic Mechanism

Vortex flow meter contains some basic parts: Bluff body of arbitrary shapes, a channel for fluidic flow and sensing body; such as piezo-electric device or micromechanical body or ultrasonic sensor etc. The bluff body, working as an obstacle in the path of fluid flow, causes the fluid to change its path and eventually generates vortices through the channel. As the frequency of the vortex is dependent on the fluid velocity, the frequency is sensed and converted to an electrical signal by a piezo-electric device which results in the flow rate of the fluid.

2.6.2 Various Forms of Vortex Flow Meters and their Mechanism

Vortex generation inside the chamber can be modified in accordance with the required direction and strength of the vortex for sensing by sensors in the flow meter. Different shapes and manipulation in the flow may produce vortices at different intensity (Alveringh, Sanders et al. 2016, Lee and Kang 2020). Different shapes change the location and strength of the vortices created inside the channel. In addition, multi-variety structures, position and the different number of the bluff body create impacts on vortex location and strength. The bluff body can be one or more than one, and its shape can be altered in triangular, rectangular, trapezoidal or half-circular and other desired

shapes. Moreover, the number and the shape of bluff bodies make differences in the flow resistance in vortex flow meters (Peng, Fu et al. 2004). With the appropriate frequency and voltage and presence of specific device or material, Clock-wise and Counter Clock-wise vortex can be produced inside low liquid flow (Shang, Huang et al. 2016).

Figure 2.11

(a) Vortex Flow Meter Diagram, (b) & (c) Different Shapes of Fluid Flow Channel (Alveringh, Sanders et al. 2016, Lee and Kang 2020)

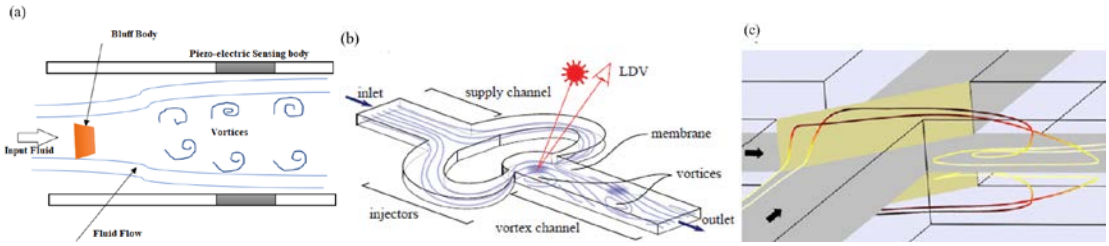

Figure 2.12

Different Configurations of Bluff Body (Peng, Fu et al. 2004)

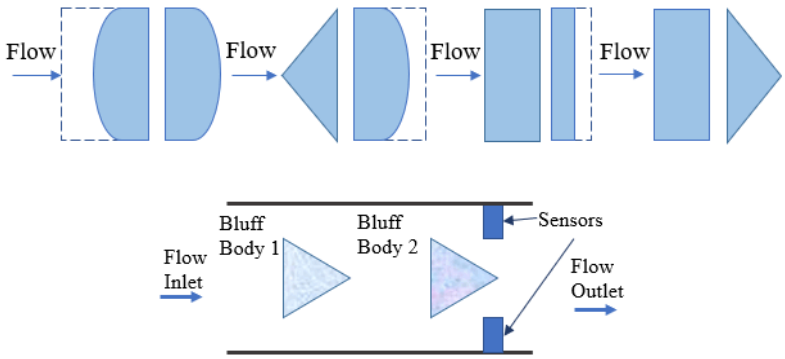

2.6.3 Advantages and Limitations

Among the micromechanical pressure sensors, the vortex flow sensor is mainly precedence for measurement of high-speed fluid velocity, viscosity, their presence and so on. But some vortex sensors are being improvised for microfluidic analysis. Though vortex sensors are helpful in flow detection, they might not be so favourable for low liquid flow in case the position of the probe is unknown within the sensor. It is due to the vortex signal being extremely insignificant compared to the ambient noise as well

as the implicit pressure. On top of that, vortex flow meters are mostly effective for clean, low viscosity liquid for their high flow rate assessment. However, observing the intensity and frequency for different trapezoidal bluff bodies, the intensity and the frequency arises with the higher flow rate for each body individually, whereas these two parameters degrade for wider bluff bodies (Zheng, Zhang et al. 2007). Compact microchip structure including microchannel can produce vortex for low flow and perform the passive mixing of chemical although the sensitivity needs to be improved further (Alveringh, Sanders et al. 2016). Besides, by means of precise design and increment in the number of the bluff body (Peng, Fu et al. 2004), microfluidic flow can be analyzed with vortex flow meters.

2.6.4 Applications

Like other micro-mechanical sensors, the vortex flowmeter is now becoming notable nowadays in the field of low flow microfluidic assessments in blood, respiratory and other organs of the biological body. Developed vortex flow meters are useful in cytometric analysis (Tovar-Lopez, Thurgood et al. 2019). Likewise, this sort of sensor is useful for analysing high velocity and low viscosity fluid: gas, vapour and liquid.

2.7 Positive Displacement Microfluidic Flow Meter

2.7.1 Basic Principle of Positive Displacement Microfluidic Flow Meter

This type of mechanical fluid flow meters can be implemented for microfluidic flow in some cases if proper modelling is done for sensing the extremely low flow rate fluid. The fundamental mechanism of a positive displacement (PD) flow meter is that while a volumetric fluid flow is passing through the meter, it creates displacements or rotations in it, which can be converted to an electrical signal by means of a piezoelectric device or transducer. Finally, this signal provides the velocity as well as the flow rate of the liquid or gas.

2.7.2 . Types of PD Flow Meter

There are several structures of positive displacement flow meter: 1. Oval gear type, 2. Nutating Disc type, 3. Piston type, 4. Rotor Vane type and (e) Sliding vane type. As mentioned earlier, normally, five types of PDs are significantly used with multiple structures of each to estimate the flow rate of a volumetric flow of fluid. The oval gear type PD flow meter consists of two similar movable valves in a perpendicular position.

While fluid crossing them originates rotations in them, which is later converted and measured in terms of flow rate. Owning almost a similar mechanism with oval gear PD, nutating disc undergoes rotation in the disc because of the circular movement of the ball in it when fluid flows through it. Here, the fluid gets equally divided into two parts of the disc volumetrically. The volumetric or rotating frequency of the disc is recorded and then converted to velocity or flow rate using a pulse transmitter. The oscillating piston type PD almost resembles the nutating disc except for the presence of an oscillating piston in replacement of the disc. The major parts of rotor vane type PD are two helical rotors; among them, one rotor sends data to the flow transmitter to measure flow rate while another helical rotor controls the pressure drop in the chamber (Smart Measurement, 2020).

Among several approaches of microfluidic applications, Squiggle micro motor PD is highly fit for insulin control via syringe. Combining the micro pump and PD method, it was proposed by *Henderson, David A* (Henderson 2007). By exploiting the cell flow or rotation, an *E. coli* MEMS-based model was prepared to control the fluid flow rate as well as cell tethering at the null level (Tung, Kim et al. 2003).

2.7.3 Advantages and Limitations

Besides handling the huge flow rate fluid, this sort of flow meters is flexible enough in measuring microfluidic flow as it can deal with both low and high viscosity fluid. Among different types of PDs, Nutating disc flow meter is desired for longer flow fluid rather than having higher accuracy (Smart Measurement, 2020). In addition, PDs do not require any input power supply. However, the main limitation of this type of flow meter is the dimension of the different sections of the meter in the case of microfluidic flow. It becomes complicated to form very small parts of the meter to deal with the low fluidic flow (ELVI FLOW, 2020). One of the microfluidic positive displacement cost-effective approaches for flow detection was proposed by *John R. Lake et al.*, which can be made within a very short period with cheap hardware and electronic mechanism providing a strong flow control (Lake, Heyde et al. 2017).

2.7.4 Applications

Positive displacement microfluidic sensors are beneficial in liquid sample collection and drug dose control phenomena (Henderson 2007). They are useful in cell flow and

nano-level fluid flow analysis as well (Tung, Kim et al. 2003). But due to shortcomings in the miniaturization of mechanical bodies, the applications of PDs are limited in certain flow profile analysis.

2.8 Coriolis Microfluidic Flow Meter

2.8.1 Basic Mechanism and Microfluidic Systems with Coriolis Force

Among the traditional Mechanical flow sensors that are gradually being miniaturized for the purpose of microfluidic measurements, the Coriolis flowmeter has been becoming popular for the last few decades in this sector. Basically, in their structure, there are two parallel tubes or pipes attached in both ends in a harmonic or a rectangular pipe with an inlet and outlet. When fluid flows through them generates a different frequency as well as Coriolis force in it which results in a path or angular deflection of these two tubes. Thus, the flow measurements: flow rate, viscosity, velocity, density, compressibility etc., are surveyed by Lorentz force on an electrical ac-current actuated in it and a magnetic field induced in the tubes (Baker 1994, Wang and Baker 2014). Due to their flexibility to any types of fluids, microfluidic applications are following an upgoing path over the course of time.

Figure 2.13

Basic Schematic of Coriolis Flow Meter (Lammerink, Lötters et al. 2011)

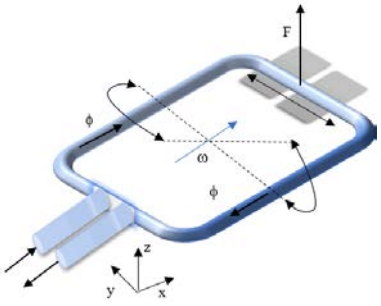

2.8.2 Types of Coriolis Flow Meter Used in Microfluidic Flow Measurement

Both straight and curved Coriolis flow meters have been being used in low flow measurement. The Eq. for curved Coriolis low flow meter was derived to show the effect of smaller size in terms of static deflection and phase difference (Ghazavi and Molki 2017). Haneveld, Lammerink et al. has demonstrated linear Coriolis low flow

meter with good accuracy resolution with a little error (Haneveld, Lammerink et al. 2008, Haneveld, Lammerink et al. 2009, Haneveld, Lammerink et al. 2010). So far, the mechanical sensors are ruling the micro and nano sensors; the Coriolis flow sensor is one of the best suited. A combination of thermal and Coriolis flow sensor was proposed by *Lammerink, Lötters et al.* (Lammerink, Lötters et al. 2011). There are many other types of microfluidic flow sensors where Coriolis flow measurement is utilized. For example, a robust and ready-to-use Coriolis flow sensor in stainless steel was achieved with a compact chip fabrication (Sparreboom, Van de Geest et al. 2013). Besides that Coriolis micro flow meter was implemented with a MEMS system (Huber 2016). Some of the implementations of Coriolis flow sensor in micro fabrication indicates a veritable possibility in the near future.

Figure 2.14

(a) Block Diagram of the Microfluidic Flow Measurement Using Thermal and Coriolis Sensor (Lammerink, Lötters et al. 2011), (b) Coriolis Flow Sensor Compacted in Electrical Circuit Along with PCB (Sparreboom, Van de Geest et al. 2013)

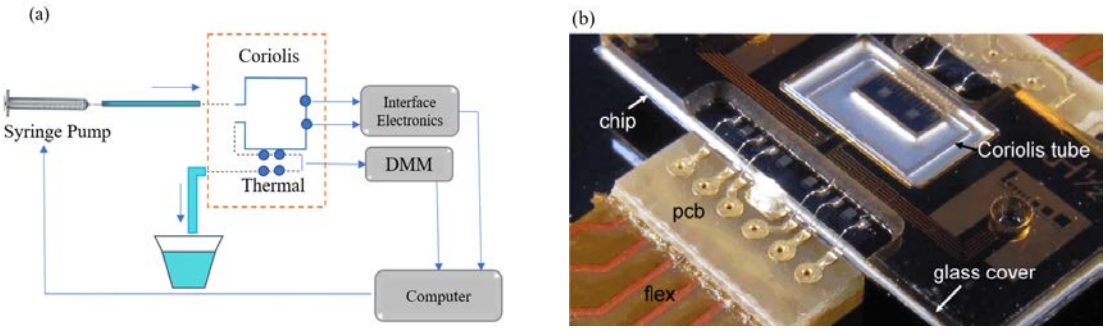

2.8.3 Advantage and Limitations

Coriolis flow sensor can assist in promoting the sensitivity to microfluidic measurement by adjusting to the thermal sensors (Lammerink, Lötters et al. 2011). Since they measure the mass flow rate directly, they can be adopted in MEMS technology to determine the density or concentration of gas or liquid in case of low flow. Also, it has been becoming a desired sensor in pressure-controlled micro devices nowadays (Alveringh, Wiegerink et al. 2017). Along with laboratory implementation, some of the micro fabricated Coriolis flow measurement sensors are now being industrialized thinly (Smith, Sparks et al. 2008, Huber 2016). To overcome the inconvenience regarding the noise and vibration in case of the mechanical pressure sensor in the microfluidic system

and develop the accuracy in the performance, the Coriolis sensor is expected to be anticipation (Alveringh, Wiegerink et al. 2018).

2.8.4 Applications

R. Smith et al. proposed silicon-based Coriolis flow sensor is applicable in the determination of very little flow rate, experiments dealing with a very small flow of fluid, pharmaceuticals, chemical analysis and so on (Smith, Sparks et al. 2008). There are different approaches adopted in the microchip functions regarding flow analysis with micro Coriolis flow sensor (Groenesteijn, Sanders et al. 2016 and Groenesteijn, de Boer et al. 2017).

2.9 Cantilever based Microfluidic Sensor

2.9.1 Basic Principle of Cantilever based Microfluidic Sensor

A micro-structured cantilever is placed perpendicularly with the flow of the fluid, and by the deflection of either piezoelectric or optical micro-resistor, the flow rate of the fluid is detected. Because while flowing the fluid through the sensor causes absorption of the molecule on the thin film of the cantilever finally bends it and therefore, deflection occurs (Lang and Gerber 2008). This sensing process can be held either in dynamic or static mode in the case of microfluidics (Walther, Fleming et al. 2015).

2.9.2 Examples of Cantilever Based Microfluidic Flow Sensor

A naïve structure for cantilever microfluidic sensor was proposed by Mohd, Omar et al., which is capable of measuring the flow rate up to 1400μL/min^{-1}. In the proposed model, a pump of porous paper was settled on the apex of the cantilever, and with mass deflection of the paper pump due to the absorption of liquid, the rate of the flow of liquid can be detected (Mohd, Sotoudegan et al. 2019). In Figure 2.15 (c), a piezoresistive cantilever-based sensing system is demonstrated where the viscosity of 3μL liquid was proposed to be measured. The attenuation from the piezoresistive array was recorded and found that for higher viscosity, the attenuation was quicker than the attenuation for lower viscosity of the liquid (Thanh-Vinh, Matsumoto et al. 2015). On the other side, optical methods for cantilever-based microfluidic sensing are becoming popular nowadays. Adopting the technique of shifting the fringe of Fabry–P´erot (FP), the flow rate from 1.3μL/min to 4μL/min can be detected with great accuracy. With the

deflection of the thin and thick cantilever, actually, the deflection occurs that results in the fringe shift (Cheri, Latifi et al. 2014). Furthermore, optically characterized cantilever-based flow sensors have been beneficial to improvise the accuracy, cost-effectivity as well as simpler techniques.

Figure 2.15

(a) A Basic Cantilever with Upper Functionalization Surface and Lower Passive Surface (Lang and Gerber 2008), (b) A Schematic of the Cantilever Setup for Measuring Flow Rates, (c) Conceptual Illustration of the Proposed Viscometer (Thanh-Vinh, Matsumoto et al. 2015)

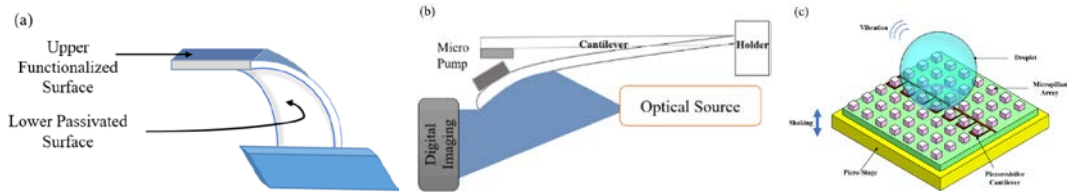

2.9.3 Advantages and Limitations

Cantilever based flow sensors have manifold advantages in biological and chemical analysis and different characterizations. Because of no requirement of o fluorescent and radioactive tags, they can be flexibly applied for nanomechanical stress measurement (Vögtli 2011). For high-speed fluidic flow, cantilever based local sensors quite effective (Salort, Rusaouën et al. 2018). Many proposed cantilever sensors are effective to sense the micro liquid flow rate, their viscosity, their presence and other features. However, there is a good number of cantilever flow sensors that are yet to be industrialized for mass production, which is not that feasible enough for practical usage. Some other phenomena, such as the higher thickness of the cantilever, hamper the sensitivity, and impure biological sample may create noise in the output (Noeth, Keller et al. 2014). Further improvements of these drawbacks may lead an extraordinary growth in their industrialization applications.

2.9.4 Applications

The cantilever based sensors, due to having a great sensitivity, have been considered beneficial for various biological and bio-medical analysis: chemical vapour deposition, viscosity and flow rate measurement, DNA hybridization detection (Lang and Gerber 2008). Again, manifold biological analysis can be done by silicon cantilever beam in their different modes (Toda, Inomata et al. 2017). Proper viscosity of sugar solution in

a biological sample can easily be determined with a micromechanical cantilever rheometer at low cost (Hennemeyer, Burghardt et al. 2008). Some other costs utilizing approaches are to measure the change in mass, and hydraulic resistance is possible with this type of sensor (Mohd, Sotoudegan et al. 2019), oil salvation using optical fibre-based cantilever sensor (Cooper, Pickrell et al. 2003) and so on. In addition, Cantilever based sensors are also convenient for drug delivery or drug location detection (Vögtli 2011). In 2013, *Ghommem, Mehdi et al.* proposed that cantilever micro sensors are capable of track out the air speed and attacking angle for aerodynamic devices: mini air craft, drone etc. (Ghommem, Calo et al. 2015). Thus, it is realized that this sensor has a promising future in numerous fields, such as biology to aerospace to chemical industries.

2.10 CNT-PDMS Based Pressure Sensors and Their Applications

The outstanding electrical, thermal, electro-mechanical behaviour of Carbon Nanotubes have made it desirable for researchers to utilize its super characteristics in order to investigate manifold phenomena from medical and health care to robotics and material property development. Due to the tremendous flexibility of the CNT-PDMS composite thin film, it has been getting popular in the wearable pressure sensors in health care applications, e.g. blood pressure, heart rate, pH level, oxygen rate measurement (Yang et al., 2018) by sensing the human body signal very precisely. These CNT-PDMS contained sensors are capable of sensing the pressure for respiratory pulse detection simply by characterizing the electromechanical characteristics of CNT (He et al., 2018) and are apt in sensitivity (Ramalingame et al., 2016) as well. Moreover, CNT-PDMS pressure sensors are now breaking new ground in biomedical sensors. For example, at the time of endovascular aneurysm repair (EVAR), it is complicated to measure the blood pressure in a very compact blood cell which is now possible with CNT-PDMS tiny pressure sensor. This sensor was demonstrated by *Sepúlveda et al.* by fabricating the homogeneous vertical CNT deposition on a substrate using Chemical Vapor Deposition (CVD) and later spreading PDMS by an acrylic mold and curing the film (Sepúlveda et al., 2011).

Besides the applications in the biomedical area, CNT-PDMS pressure sensors have been getting notable in robotics and soft wearable electronics. In 2017, *Yoon & Chang* a capacitive CNT-PDMS pressure sensor, was introduced to detect and differentiate the

human touches and change in temperature (Yoon & Chang, 2017) using the capacitive change with pressure. On the other hand, resistive and pressure or electromechanical behaviour of CNT-PDMS composite is used in very small pressure detection (Yogeswaran et al., 2015), which is much smaller than soft human touch. Again, CNT-PDMS film can be used to detect the gesture and grip of the robot. For this purpose, the homogeneous distribution of CNT into PDMS is highly required. Therefore, CNT is first dispersed into a solvent, and after sonication or magnetic stirring, PDMS is added to have magnetic stirring again, and at the end, with the curing agent, it is cured in the desired mold with electrodes (Rajarajan Ramalingame, Lakshmanan, Müller, Thomas, & Kanoun, 2019). Again, by means of increasing the dielectric properties of CNT-PDMS and utilizing capacitive characteristics, sophistication in the robotic skin or gait (Jang et al., 2016) can be achieved. The film with PDMS polymer does not have any conductivity. They are increasing the amount of conductive MWCNT into PDMS matrix results in conductivity. However, initially, when the percentage of carbon nanotubes in the PDMS matrix is inferior for fewer weight percentage, there is no conductivity found. Significant conductivity is shown after around 7-8wt% of MWCNT into PDMS. And later, with the increase of MWCNT percentage, gradually, the conductivity increases as the resistance decreases (Yogeswaran, Khan et al. 2015). The thickness of the film also affects the conductivity of the film. For the higher thickness of the film, conductivity is higher. All in all, it is visible that CNT-PDMS pressure sensors have been getting demanding in micro devices due to their magnificent electro-mechanical characteristics.

2.11 Summary

Eventually, after the detailed overview of the low flow sensors, it can be concluded that the mechanical pressure sensors are easier to operate as well as simpler in terms of their fabrication in comparison to optical, thermal and electromagnetic flow sensors. In addition, micro pressure sensors are free from the impairment of heat, which is a labyrinth in the case of some thermal low flow meter. Moreover, optical-based flow sensors illustrate obstacles in terms of transmission of specific wave in a very confined micro channel which is again not an obstruction for the low fluidic flow pressure sensor. On top of that, specifically, in the literature, the cantilever based pressure sensor used for low fluidic flow assessment was more complicated approaches mixing up with optical (Mohd, Sotoudegan, Ligler, & Walker, 2019; Walther, Fleming, Padovani, &

Hegner, 2015), electro-mechanical systems (Salort et al., 2018; Toda, Inomata, Ono, & Voiculescu, 2017). Again, in this research, a very simple method to prepare the CNT based PDMS will be demonstrated.

In this thesis, the development and investigation of low flow rated fluid carried by a very small (D = 5mm) channel containing MWCNT based PDMS polymer has been carried out. A thoroughly simple but effective approach with a dapper design and orientation of MWCNT composite PDMS polymer film inside a hollow cylindrical closed channel was proposed to measure a very low flow rate of the liquid. To characterize the flow rate in terms of bending, the change in current was considered to analyze the system behaviour. However, the system was not tested for various types of liquids and also the sensor fabrication was limited to only using PDMS polymer. The testing will be conducted only using DI water to check the system behaviour for different flow rates.

CHAPTER 3
METHODOLOGY

The overall outline of the research methodology is broadly divided into four sections, as shown below. Briefly, the initial part of the research will focus on the preparation of the MWCNT-PDMS composite thin film. Afterwards, the characterization of the film is represented, which includes the electrical, mechanical and electro-mechanical behaviour of the MWCNT-PDMS film. These characterizations will be essential to understand the behaviour of the MWCNT-PDMS sensor to implement into the system. Finally, the fabrication of flow channel will be fabricated, and the sensor film will be placed inside the device to measure the flow rate of liquid flowing through the device. The glimpse of the methodology that will be adopted in this thesis work is exhibited in Figure 3.1.

Figure 3.1

A Short Overview of the Research Methodology

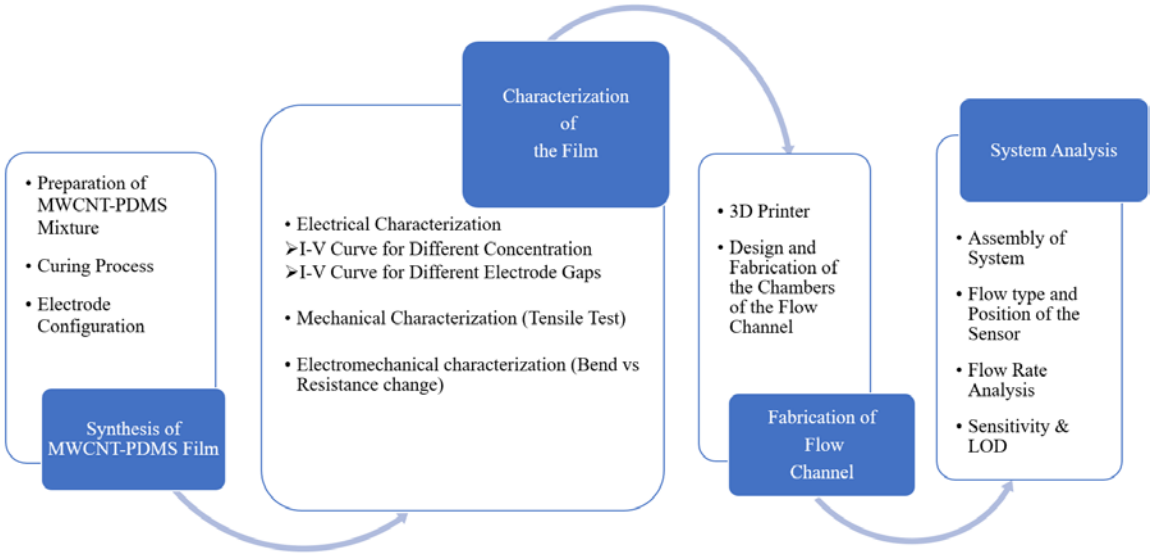

3.1 Synthesis of MWCNT-PDMS Composite Polymer Film

3.1.1 Preparation of MWCNT-PDMS Mixture

A homogeneous mixture of MWCNT and Polydimethylsiloxane (PDMS) is to be prepared for the preparation of the sensor film. For this purpose, the following steps are followed. In the case of only PDMS film, 1 gram of PDMS base was mixed with 0.1

gram of curing agent, which is 10% of the base. Then they were mixed under magnetic stirring at 300 rpm for 15 minutes. If there is any bubble in the mixture, the mixture was placed into the vacuum chamber for about 10 minutes before curing. On the other hand, for 0.1wt%, 1wt%, 5wt%, 8wt%, 10wt%, 12wt%, 15wt% and 20wt%, 1 gram of PDMS base was taken into a beaker, and MWCNT was added according to the weight percentage of the MWCNT (Table 3.1). Afterwards, they were mixed homogeneously using magnetic stirring for about 15 minutes (Figure 3.2). Later, the curing agent was added to it with a weight percentage of 10% of the base, which is 0.1 g. However, in the case of weight percentage above 8wt%, it is hard to mix appropriately and homogeneously due to a higher percentage of MWCNT into PDMS. Therefore, two spatulas were used to mix them homogeneously.

Table 3.1

Amount of MWCNT for Different Weight Percentages

Weight Percentage	Amount of MCNT
0wt%	0 g
0.1wt%	0.001 g
1wt%	0.01 g
5wt%	0.05 g
8wt%	0.08 g
10wt%	0.1 g
12wt%	0.12 g
15wt%	0.15 g
20wt%	0.2 g

Figure 3.2

The Process of Preparation of MWCNT-PDMS Homogeneous Mixture

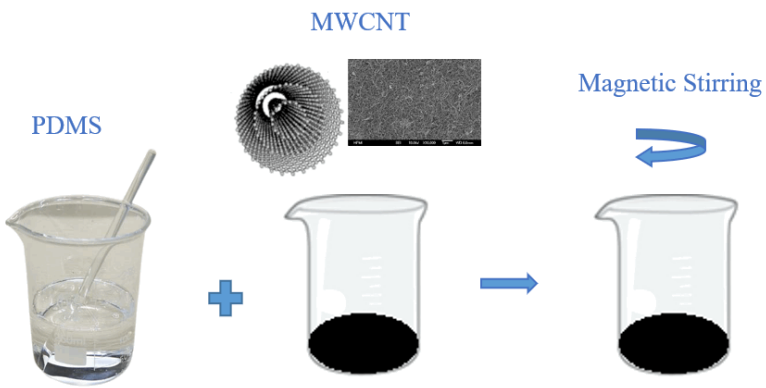

3.1.2 Curing Process of the Film

The homogeneous mixture of MWCNT-PDMS was spread on a mold made up of a glass slide with the help of a roller or spatula. The base of the mold is made up of a glass slide where the height of 0.5 mm on its top was made by using three layers of double-sided tape as each layer of this tape is approximately 0.167 mm. The dimension of the mold was varied according to the requirement of the film dimension. For example, in order to prepare the MWCNT-PDMS film samples for the tensile test, the dimension of the films was 50 mm* 10 mm* 0.5 mm. On the other side, the samples that were used in the system as the reference sensor and the testing sensor had different dimension which was 15 mm* 3.5* 0.5 mm. After spreading the MWCNT-PDMS mixture on the mold, it was placed into an oven under 80°C for 2 hours and the film was peeled off from the mold.

Figure 3.3

Mold for Film Preparation (a) Without MWCNT-PDMS Layer, (b) With MWCNT-PDMS Layer (c) MWCNT-PDMS Film

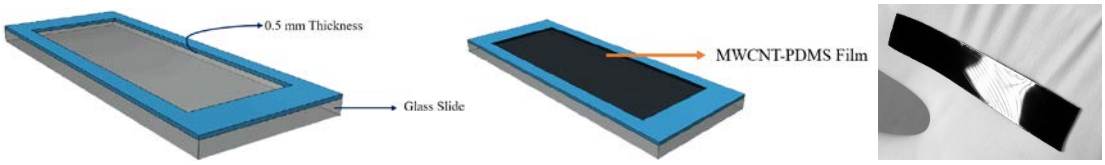

3.1.3 Electrode Configuration

For the electrical characterization of the film, as well as to measure the current changes in the system, two electrodes were placed inside the film. The material of the electrodes was used Aluminum foil, and the aluminium sheet was rolled up into three to four layers to give it a strong form. The width of the electrodes was around 1 mm. Two types of combinations of the electrodes were used for these two purposes. The first combination is shown in Figure 3.4 (a); two electrodes were placed parallel to each other on the film. The film with this configuration of the electrode was used to perform the electrical characterization. Another configuration of electrodes illustrated in Figure 3.4 (b) was used for system characterization. The smaller gap was kept in the vertical distance, where a larger gap was maintained in the horizontal distance. The resistance of the film was controlled by the smaller gap rather than a bigger gap of the electrodes. On top of that, different gaps between the electrodes were maintained, putting 3D rectangular

structures in between the electrodes, as demonstrated in Figure 3.4 (c). After the placement of the electrode, the distance maker structure was removed.

Figure 3.4

Electrode Configuration for (a) electrical Characterization (b) System Usage (c) Gap Maker Between the Electrodes

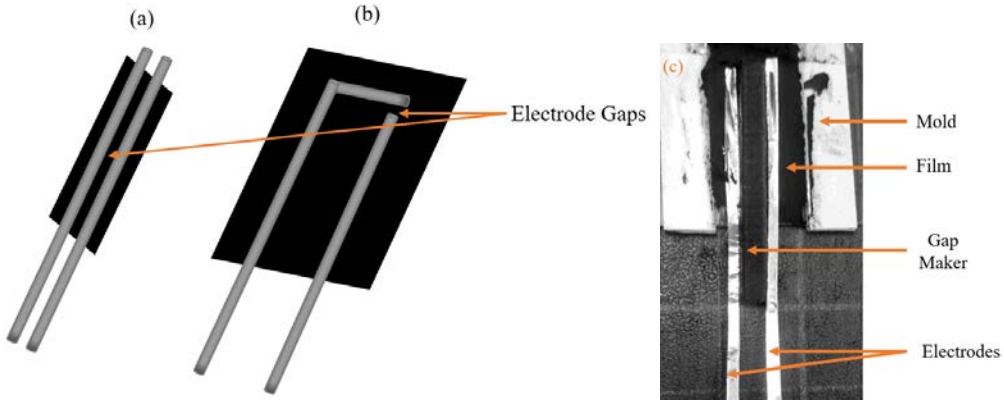

3.2 Characterization of the MWCNT-PDMs Film

3.2.1 Electrical characterization

The conductivity of the film was checked using an electrometer. Two electrodes of the film were connected to the two terminals of the electrometer. The programmable electrometer basically worked as a multimeter which is capable of measuring the voltage provided to the film and the current flowing through it. The voltage was varied from 0V to 3V with an interval of 0.05V, and the corresponding currents were recorded accordingly. In order to understand the conductive behaviour of the sensor film, the currents against the voltages were recorded for different concentration of MWCNT-PDMS, e.g. 0wt%, 0.1wt%, 1wt%, 5wt%, 8wt%, 10wt%, 12wt%. For a lower concentration of MWCNT into PDMS, The PDMS matrix dominate over MWCNT; thus, the electrodes may not get in touch with MWCNT, which will result in no conductivity shown for the film. However, for the higher concentration of MWCNT, it will dominate over the PDMS matrix, and more MWCNT will get contact with the electrodes. Therefore, for a higher weight percentage of MWCNT, the conductivity of the film will be exhibited. Moreover, the I-V curves for different electrode gaps for 10wt% and 12wt% film were generated to illustrate the electrical characteristic of the sensor film. Higher electrode gaps provide higher resistance to the film.

Figure 3.5

Schematic of the Electrical Characterization Setup

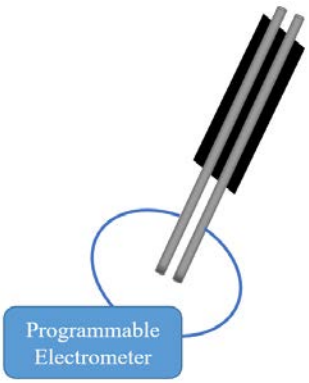

3.2.2 Mechanical Characterization of the Film

Due to the requirement of having the flexibility in the MWCNT-PDMS film for sufficient bending, the tensile test of the films with different concentrations were conducted. The batches of different concentration of MWCNT-PDMS film, including three identical samples each, were prepared. The dimension of each film was 50 mm*10 mm* 0.5 mm in terms of length, width and thickness Figure 3.6 (a) & (b). Each sample was tested, and the results of three identical samples were averaged to get the accumulated result. The tensile tests were performed using Texture Analysis Machine Figure 3.6 (c) in NCTC (NSTDA Characterization and Testing Service Center (NCTC)) in NSTDA (National Science and Technology Development Agency).

Figure 3.6

(a) Identical PDMS Films (b) Identical MWCNT-PDMS Films (c) Texture Analysis Machine

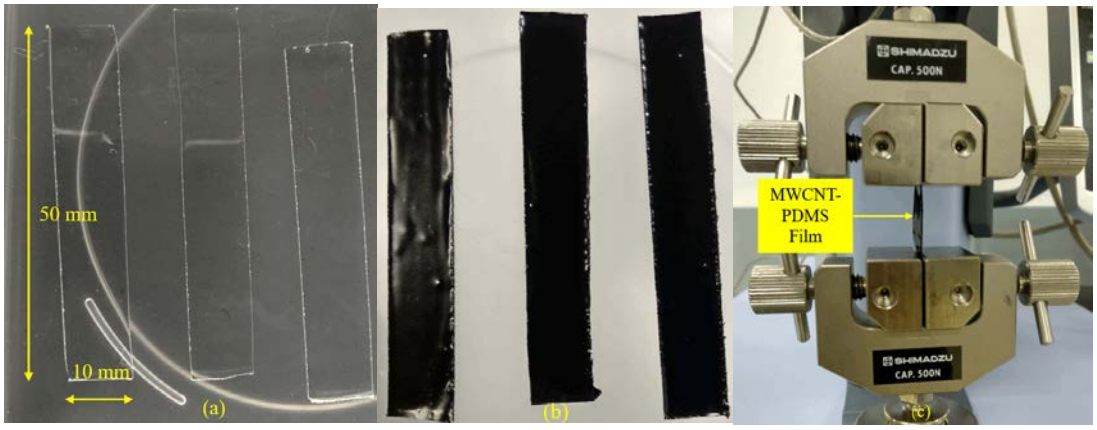

The grip on each side of the films was 15 mm, and the gauge length was 30 mm. The speed of the stroke was maintained at 25 mm/ min. The tensile tests were performed for only PDMS, 0.1wt%, 1wt%, 10wt%, 12wt% and 15wt% MWCNT-PDMS films. The stress vs strain curves was generated from the test for three identical samples, and the average of them was considered. It was noticed that in the case of all batches of samples, the stress vs strain curve came out only at the elastic region, which indicates that the PDMS or MWCNT-PDMS films are elastic as well as flexible. This property of the film is beneficial for utilizing the bend of the film for a different flow rate of the liquid. The Elasticity Modulus was calculated from Eq. (3.1). Elasticity Modulus (MPa),

$$E = \frac{FL}{A\Delta L} \ldots\ldots\ldots\ldots \text{(Eq. 3.1)}$$

Where F is the force, L is the initial length of the film, A is the area of the film and ΔL is the displacement after achieving the break-point of the film. The elastic region of any sample is mostly linear; thus, the slope can be considered as Young's modulus or the elastic modulus.

3.2.3 Electro-Mechanical Characteristics of the Film

The changes in the resistance due to a very small bending were observed in the MWCNT-PDMS films, where the electrode gap in the films was kept 1 mm. The resistance changes due to the bending as the electrode gap changes with it. The change of resistance was observed from 0° to 3° bending with an interval of 0.5°.

Figure 3.7

Setup for Electromechanical Characterization

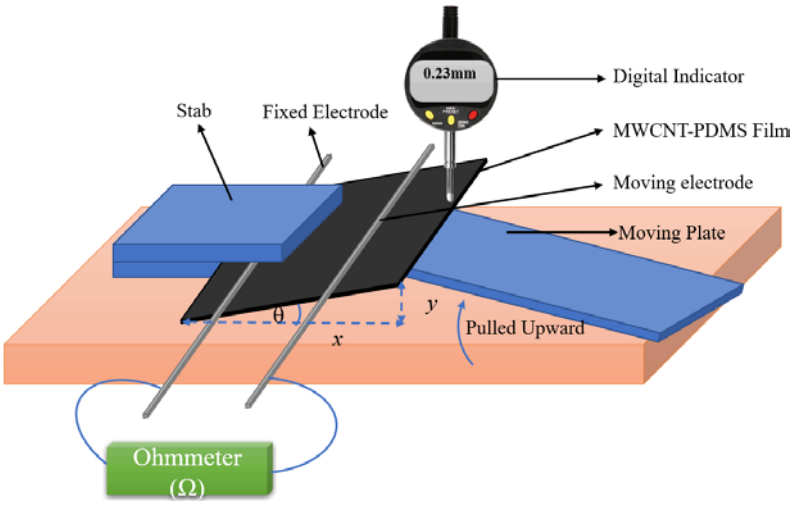

One side of the film with one of the electrodes was stabbed, and the other side of the film with the other electrode was getting bent. The horizontal length (x) was fixed, which is actually the width of the film, and the vertical displacement (y) was measured using a digital indicator. Later, using Eq. (3.2), the bending angle was calculated. For bend in the film, the gap between the electrodes increased, which resulted in a decrease in the current through the film. The voltage was kept fixed to a certain value, and the current changes were recorded using an electrometer.

$$\theta = \tan^{-1}\frac{y}{x} \quad \text{..... (Eq. 3.2)}$$

3.3 Fabrication of Flow Channel

3.3.1 3D Printer

A flow channel including one upper chamber and one lower chamber was fabricated using a Wanhao 3D printer. The designs of both chambers were drawn in 123D Design software. Later, the designs were converted into an 'STL' file to make it readable in Wanhao software. The STL file then converted into 'G-code' using the Wanhao software and transferred into an SD card provided by the 3D printer.

Figure 3.8

Wanhao 3D Printer Used for Flow Channel Fabrication

The upper chamber took 45 minutes, where the lower chamber was printed within around 1 hour 30 minutes. After finishing the printing, the bed temperature and the

extra temperature were increased to 80°C and 250°C respectively in order to make contact between the bed and the printed structure lose, which helps the structure to be pulled out easily.

3.3.2 Chambers of the Flow Channel

The flow channel consists of two chambers; the upper chamber and the lower chamber. The upper chamber is a 3D rectangular shape of 50 mm, 10 mm and 17 mm in length, width and height, respectively. It also consists of the flow channel with a diameter of 3 mm, 5 mm and 7 mm for individual requirement. In the upper chamber, the bottom part has rectangular hollow spaces where the sensor holder from the lower chamber can be inserted and thus can provide a closed channel. In the lower part of this chamber, there are two rectangular hollow places where some portion of the lower chamber can be inserted.

Figure 3.9

Upper Chamber (a) Overall View (b) Side View (c) Bottom View

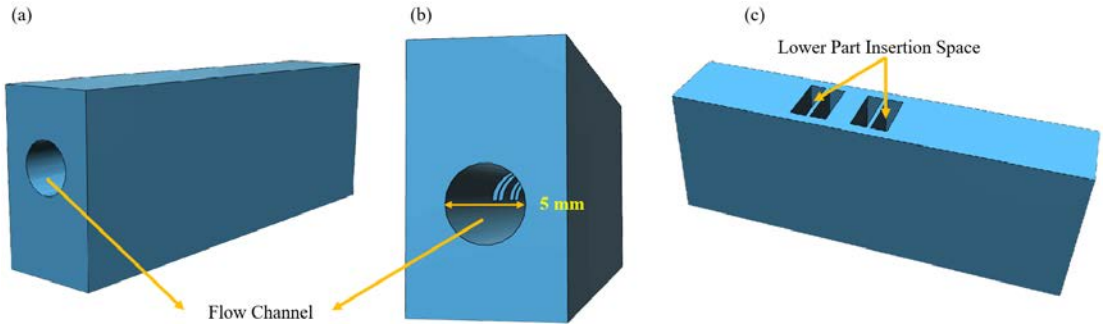

On the other side, the lower chamber is a 3D rectangular shape of 60mm*20mm*8mm outer dimension and 50mm*10mm*3mm inner dimension. There are two cases for holding the reference sensor and testing sensor. Each of the holding slits is 5 mm, 2 mm and 10 mm in length, width and height, and the gap between the two corresponding slits are 0.5 mm, which is basically the thickness of the sensor film. The distance between the reference case and the testing sensors case is 10 mm. The sensors are inserted through the space of the bottom (Figure 3.10 (c)), and the electrodes are kept hanging outside of the structure. The structures were designed using ‘123D design’ software and fabricated using ‘Wanhao 3D printer’. The material of the structure used in the 3D

printer is Polylactic Acid (PLA) which is one kind of acrylic polymer with black colour, quite hard texture and lightweight.

Figure 3.10

Lower Chamber (a) Side View (b) Top View (c) Bottom View

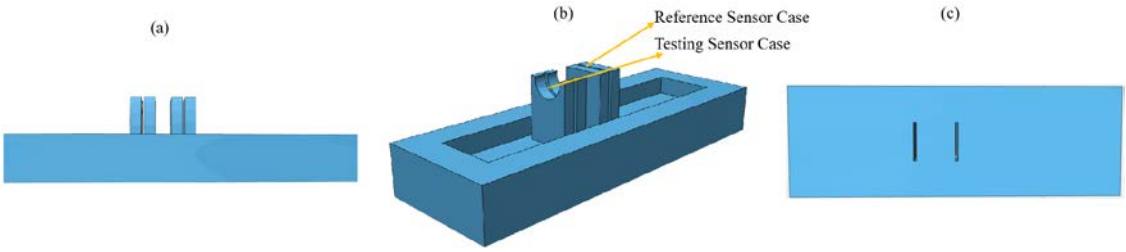

3.4 System and Flow Rates

3.4.1 Assembly of the System

At first, the testing sensor and the reference sensors are placed inside their assigned cases in the lower chamber, where their electrodes are kept outside of the chamber. The electrodes are connected to the electrometer to measure the currents. The upper chamber was placed on top of the lower chamber to make the system closed. The top end of the testing sensor was exposed to the flow channel of the upper chamber. On the electrode of the testing, the sensor was stabbed with the case of the lower chamber, and another electrode was kept free to bend in the flow channel. The reference sensor was kept hidden into its case, unaffected by the flow through the channel.

Figure 3.11

(a) Lower Chamber (b) Bottom View of Upper Chamber (c) Complete Chamber

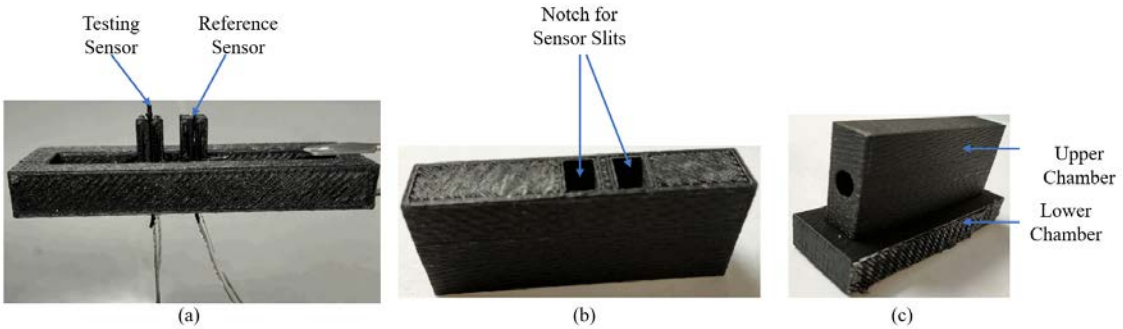

A bottle of liquid was hanged with a stand, and a pipe through which the liquid passed was connected with an infusion pump. The outlet of this flow pipe exiting from the infusion pump was inserted into the flow channel. When there was no flow, the current was almost the same. However, when there was a flow through the channel, due to different flow rates, there were different force as well as pressure applied on the testing sensor, which made different bending angle to the film resulting in different changes in the current. Therefore, the flow rates of the liquid can be analyzed by means of the change in current for the different bending angle of the testing sensor. The flow rates can be varied from 0mL/h to 995 mL/h using the infusion pump for different volume of the liquid.

Figure 3.12

Schematic of the Overall System to Measure the Flow Rates of the Liquid

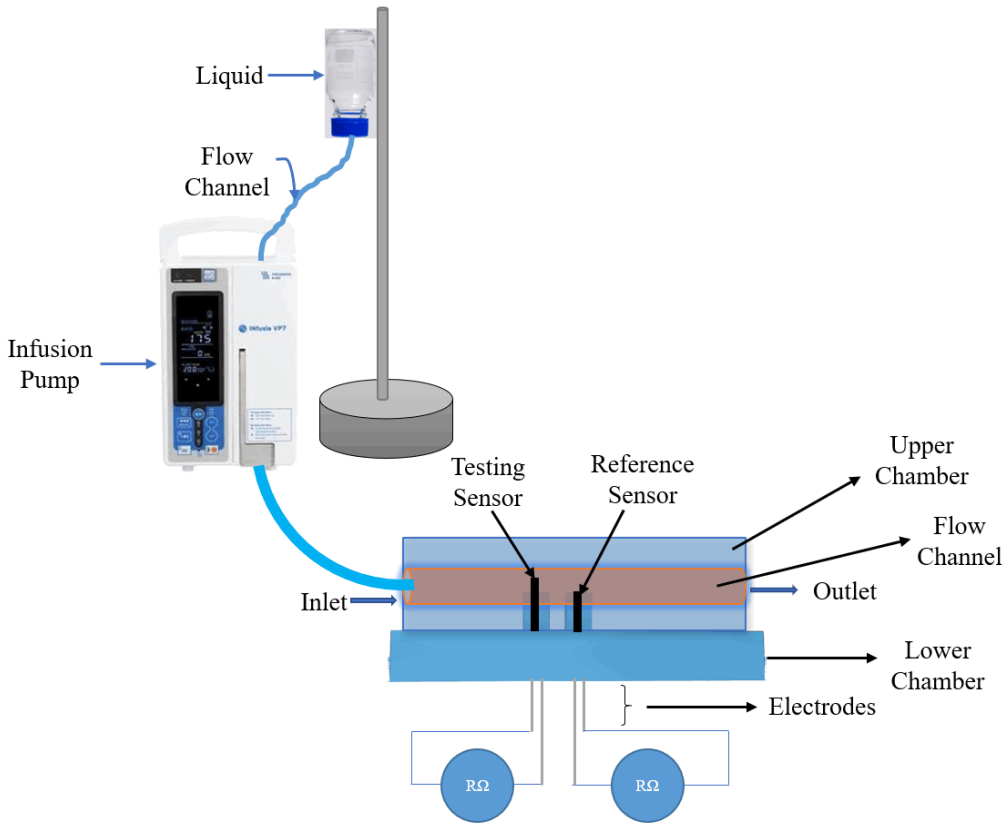

3.4.2 Flow Type and Position of the Sensors

Identification of the liquid flow type is important to measure the loss in pressure inside the flow channel to avoid the impact of the loss on the bending angle as well as the

current changes. For this purpose, Reynold number (R_e) should be calculated as this constant represents the type of flow. If the value of R_e is less than 2300 indicates laminar flow, and for laminar flow, the friction factor can be calculated from Eq. 3.3, which is beneficial to find out the head loss as well as the pressure drop. These are important to calculate because head loss and pressure drop may affect the phenomenon to occur similar bending due to different pressure drops. And also, Reynold number is necessary as different types of liquid flow behave in a different manner to apply pressure on the sensor and results in different bending.

Reynold Number, $R_e = \frac{\rho v D}{\mu}$ …… (Eq. 3.3)

Friction Factor, $f = \frac{64}{R_e}$ …… (Eq. 3.4)

Head Loss, $h_L = \frac{fLv^2}{2Dg}$ …….. (Eq. 3.5)

Pressure Drop, $P_L = \rho g h_L$ …… (Eq. 3.6)

Moreover, from the fluid mechanics it is known that the velocity as well as the applied pressure due to any velocity is maximum in the center of the channel. Therefore, the free end of the testing sensor was kept in the center position and placed closer to the inlet so that it can be provided with enough force to bend and exhibit appropriate changes in current. For a specific flow rate, the average and standard deviation of current changes were calculated from the data from Eq. (3.7 and 3.8). Finally using Eq. (3.9), the limit of detection was found.

Average Current Change, $\Delta I_{average} = \frac{\sum_{i=1}^{n} I_i}{n}$ ……. (Eq. 3.7)

Standard Deviation, $I_{std} = \sqrt{\frac{\sum_{i=1}^{n}(I_i - I_{average})^2}{n}}$ …… (Eq. 3.8)

Limit of Detection, $LOD = \Delta I_{average} + 2 * I_{std}$ ……. (Eq. 3.9)

$Sensitivity = Slope = \frac{y}{x} = \frac{\Delta I_{average}}{FR}$ …….. (Eq. 3.10)

Where, $\Delta I_{average}$, I_{std}, FR and n are average change in the current, standard deviation of current changes, flow rate and the number of repetitions, respectively.

CHAPTER 4
RESULTS AND DISCUSSION

This chapter describes the properties of the MWCNTs used in this study and the results of the conducting MWCNT-PDMS thin films prepared at different concentrations of MWCNTS and their characterization, including their electrical and mechanical properties. The chapter then discusses the implementation of the conducting MWCNT-PDMS thin films into a fluid flow sensor and describes the results obtained for the sensor at different flow rates of water inside a flow channel. The sensing mechanism is described, and the sensitivity and limit of detection (LoD) of the sensor are discussed. A laboratory-scale prototype of the developed sensor is demonstrated at the end, and its performance under different flow rates is discussed.

4.1 Characteristics of the MWCNTs

4.1.1 Size of the MWCNTs

In order to investigate the size of the MWCNTs used in this research, scanning electron microscopy (SEM) was performed. Figure 4.1 (a) shows the SEM micrographs of the MWCNTs at 100k magnification. The MWCNTs showed their typical curved cylindrical tube-like structure but found in an entangled configuration which is common since these MWCNTs were used as received without any chemical surface modifications. The diameters of the MWCNTs have spread approximately between 20 nm to 60 nm, as illustrated in Figure 4.1 (b), with an average diameter of 39.4 nm ± 21.4 nm estimated from 50 different nanotubes.

Figure 4.1

(a) SEM of MWCNT at 50k SE (b) Frequency Distribution of MWCNT Diameter

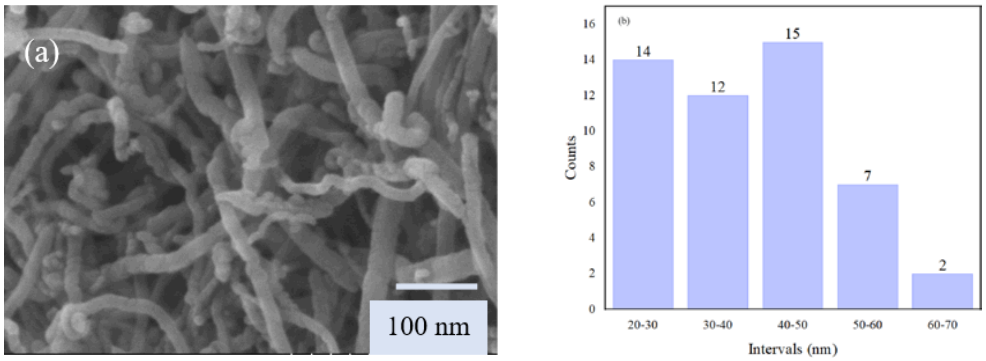

4.1.2 Raman Analysis of MWCNTs

For the purpose of analyzing the structural quality of the MWCNTs, Raman Spectroscopy was conducted using a confocal Raman spectrometer. Figure 4.2 shows the Raman spectrum of the MWCNTs recorded with 532 nm laser excitation, where three characteristic Raman features of CNTs can be observed. The Raman band peaking at around 1571.83 cm^{-1} corresponds to the *G*-band of the nanotubes representing the longitudinal optical (LO) phonon mode of CNTs. The *D*-band is also known as the defect or disordered mode due to the fact that defects, such as in-plane substitutional hetero-atoms, vacancies, grain boundaries, or other defects, are required to observe this band.

Figure 4.2

Raman Spectrum of the MWCNTs used in This Study

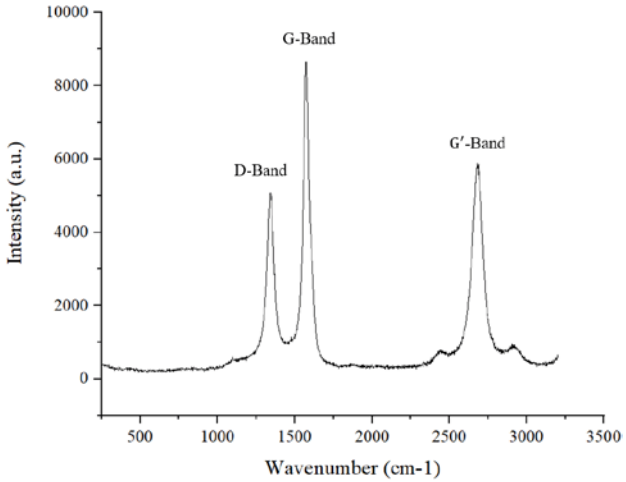

A strong *D*-band observed in our sample indicates that the MWCNTs used in this study contains a significant number of defects them which is common in metallic MWCNTs. The Raman band peaking at around 1571.83 cm^{-1} is due to the tangential shear mode of carbon atoms that corresponds to the stretching mode in the graphitic planes of the MWCNTs. This band is known as *G*-band, and it is the most prominent Raman characteristic of CNTs which is also observed in simple graphite. The quality of MWCNTs have often been evaluated using the *D/G* band intensities, and generally, this ratio is less than 2% for high-quality CNTs without defects and amorphous carbon. In our MWCNTs, however, the *D/G* ratio was found around 40%, indicating the presence of a significant number of defects that can lower the crystal symmetry of the quasi-

infinite lattice. The Raman band observed at higher frequencies peaking at around 2684.25 cm^{-1} is assigned to the *G'*-band of CNTs, which is an intrinsic property of the nanotubes related to their LO phonon modes. This band is also known as 2*D*-band and generally occurs close to twice that of the *D*-band.

4.2 MWCNT-PDMS Composite Thin Film

4.2.1 Different Concentration of MWCNT-PDMS Mixture

Different concentrations of MWCNT-PDMS mixture were prepared initially to analyze their character and to select the best fitting film for the sensor system. 0wt% (only PDMS), 0.1wt%, 1wt%, 5wt%, 8wt%, 10wt%, 12wt%, 15wt% and 20wt% of MWCNT-PDMS mixtures were prepared by following a simple mixing method as described in Chapter 3. For 0.1wt%, 1wt% and 5wt% and 8wt%, 0.1 g, 1 g, 5 g and 8 g of MWCNT were added respectively to 1 g of PDMS base and put under magnetic stirring for 15 minutes under 300 rpm rotation speed. From 0wt% to 8wt% MWCNT-PDMS ratio, it was easy to mix the MWCNT powder to PDMS base homogeneously (Figure 4.3) by magnetic stirring.

Figure 4.3

Mixture of MWCNT and PDMS base for (a) PDMS (b) 1wt% (c) 5wt% (d) 8wt% (e) 10wt% (f) 12wt% (g) 15wt% and (h) 20wt%

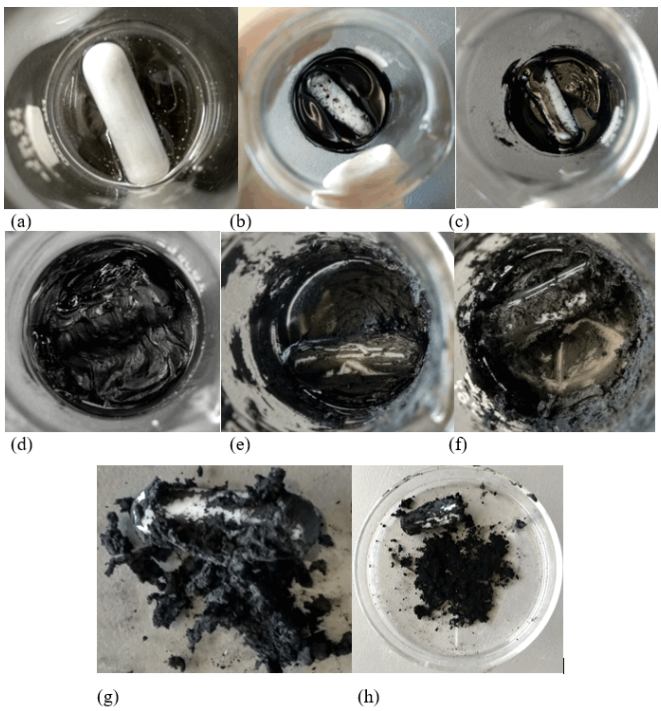

However, with the increase in the MWCNT concentration, e.g. 10wt% and 12wt%, only magnetic stirring was not enough to get a homogeneous mixture. Rather after the magnetic stirring, the mixture was again properly stirred one spatula by hand stirring until having a homogeneous texture. Further increase in the MWCNT weight percentage, such as for 15wt%, it was hard to get a homogeneous mixture even after magnetic and hand stirring since the amount of MWCNT started dominating the PDMS matric. For 20wt%, it was not possible to mix the MWCNT and PDMS base and mostly, the MWCNT stayed in either lumped or powder form. After getting the homogeneous mixture of MWCNT and PDMS base, the curing agent was added to the mixture in an amount of 10% of the PDMS base and mixed further under magnetic and hand stirring. For example, if the amount of PDMS base was 1 g, the amount of curing agent was taken 0.1 g, and it was changed accordingly with the amount of PDMS.

4.2.2 Curing of MWCNT-PDMS Film

After the mixing process, the mixtures were spread on a mold using a roller for lower concentration and a spatula for higher concentration. The dimension of the mold was changed according to the requirements of the film dimension. Three different batches of MWCNT-PDMS films were prepared. The dimensions of the molds for the films required for tensile test, I-V characteristic analysis and film for the system are mentioned in Table 4.1.

Table 4.1

Dimensions of the Prepared MWCNT-PDMS Film

Purpose of the Usage	Length (mm)	Width (mm)	Thickness (mm)
Tensile Test	50	10	0.5
Electrical Characterization	20	5-12	0.5
Implementation in the System	20	5	0.5

Three layers of white double-sided tape were used to make approximate 0.5 mm thickness which was measured by Vernier calliper. After spreading the MWCNT-PDMS mixture on the mold, it was placed into the oven for 2 hours under 80°C and the film were formed likewise. The mixture was spread on the mold either by using a roller

or spatula. For a lower concentration of MWCNT, the mixture is not that stiff. Therefore, it was easier to spread on the mold with the help of a roller. However, since with the increased weight percentage of MWCNT into the PDMS matrix, it becomes hard to spread. On that occasion, a stainless-steel spatula was used to spread homogeneously on the mold.

Figure 4.4

(a) MWCNT-PDMS Mixture on the Mold (b) MWCNT-PDMS Film

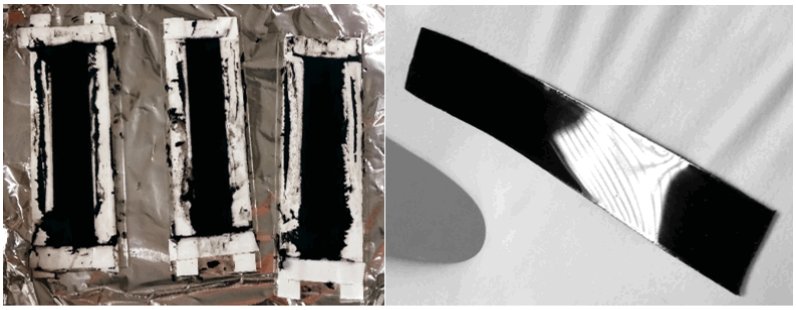

(a) (b)

4.3 Characterization of the MWCNT-PDMS Film

4.3.1 Contact Angle

The contact angle for different concentrated CNT- PDMS film was observed using a water droplet on the surface of the film. It was found that in most of the cases, the water contact angle was greater than 90° which implies that the PDMS, as well as the CNT-PDMS films analyzed in this study, are hydrophobic. For example, the average water contact angle for PDMS was found at 107.5°. The water contact angle keeps on increasing with the increase of the concentration of CNT into PDMS. Figure 4.5 shows the average water contact angle of different concentrated CNT-PDMS film. It represents that the average water contact angle increases with a higher weight percentage of CNT into PDMS film. For example, the average water contact angle increased from 107.5° to 128.57° for the increase in the concentration of MWCNT from 0wt% to 12wt%. Therefore, it can be said that the hydrophobicity of the film improves with the increased amount of CNT. In the system, when there will be a flow of water, it will not stay stick to the film due to its hydrophobic nature on the surface of the film if a highly concentrated CNT-PDMS film is selected.

Figure 4.5

Contact Angle for (a) 0wt% (b) 0.1wt% (c) 10wt% (d) 12wt%

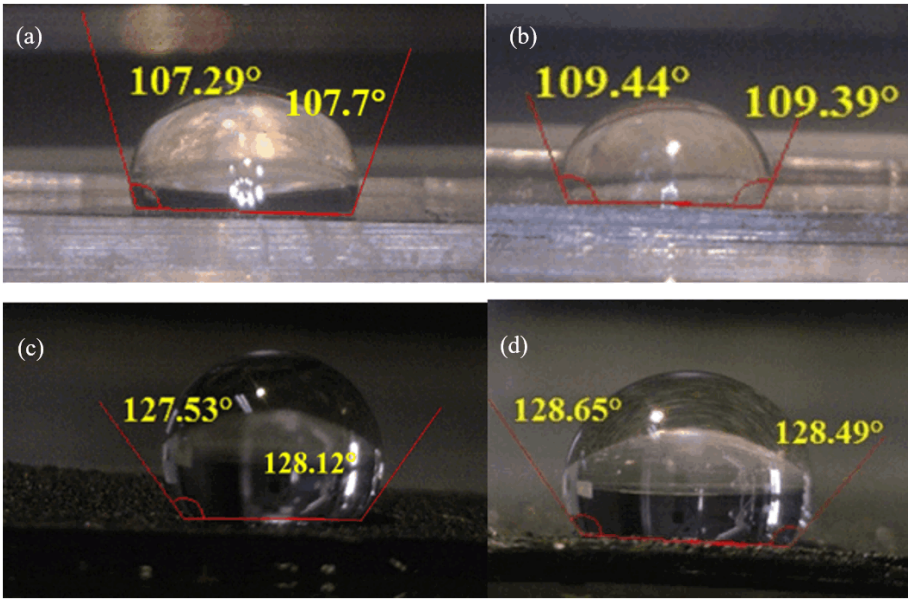

Table 4.2

Water Contact Angle for Different Concentration of MWCNT-PDMS Film

Concentration	Left Side Contact Angle (°)	Right Side Contact Angle (°)	Average Contact Angle (°)
0wt%	107.29	107.7	107.5
0.1wt%	109.4	109.39	109.4
1wt%	119.31	119.54	119.43
5wt%	123.18	123.79	123.49
10wt%	127.53	128.12	127.83
12wt%	128.65	128.49	128.57

4.3.2 Electrical Characterization of the MWCNT-PDMS Film

In Figure 4.6 (a), it is illustrated that for a higher weight percentage of CNT-PDMS ratio, the conductivity as well as the current through the film significantly elevated. Because with a higher percentage of MWCNT, it started dominating the PDMs matrix and get into contact with the electrodes. Moreover, due to the higher electrode gaps for individual, the conductivity, as well as the resistance, gradually increased. Figure 4.6 (c) illustrates MWCNT-PDMS films with different electrode gaps from 0.5 mm to 10 mm. Two to three layers of aluminium paper were used as the electrodes. In Figure 4.6

(d) and (e), the change in conductivity or current for different electrode gaps for 10wt% and 12wt% is demonstrated, respectively. The current is almost twice in 12wt% than in 10wt% for specific voltage provided to the films. For example, for a fixed voltage, the amount of current flows through the 10wt% film became almost twice in the case of 12wt% MWCNT-PDMS film. Therefore, if the film with a 12wt% MWCNT-PDMS ratio can be utilized in the final system as the testing as well as the reference sensor, significant changes can be recorded and analyzed, which will be more convenient than using 10wt% film.

Figure 4.6

(a) MWCNT-PDMS Film with Different Electrode Gaps (b) I-V Curve for Different Concentrations of MWCNT (c) I-V Curve for Different Electrode Gaps in 10wt% MWCNT-PDMS Film (d) I-V Curve for Different Electrode Gaps in 12wt% MWCNT-PDMS Film

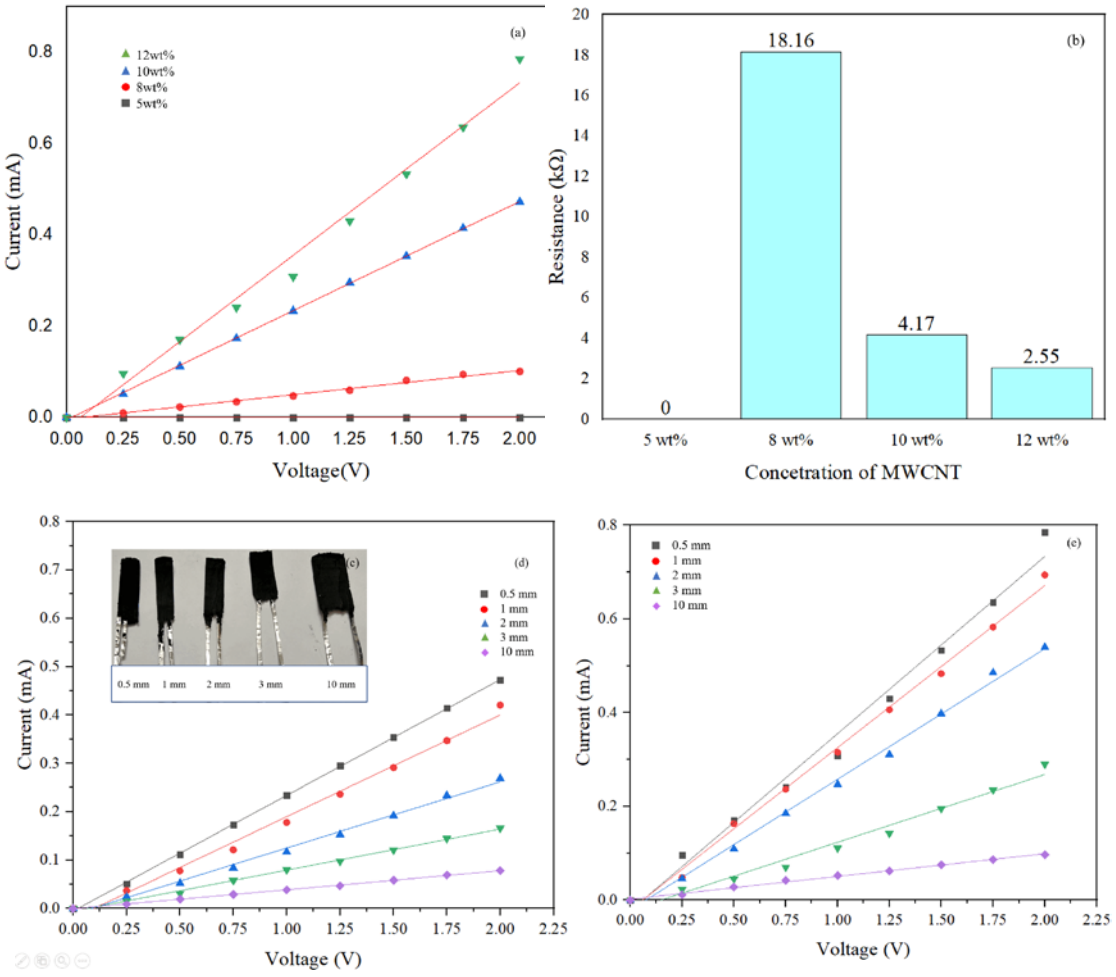

The change in resistance with respect to the concentration of CNT into PDMS film was recorded. The gap between the electrodes was kept at approximately 0.5mm, and the thickness of the film was 0.5mm. It was recorded that for 0wt%, 0.1wt%, 1wt% and 5wt%, there was no conductivity shown, where for 8wt%, conductivity was exhibited with a resistance of around 18.16 kΩ. Periodically, the conductivity of the film started uplifting as the concentration was being stepped up with a decrease in the resistance. For example, when the concentration was heightened to 10wt% as well as 12wt%, the resistance resulted in 4.17 kΩ and 2.55 kΩ, respectively.

4.3.3 Mechanical Characterization of MWCNT-PDMS Film

The tensile test of the film provided information regarding the texture strength of the film. Because the tensile test provided the stress vs strain curve from where the response region illustrates whether the film is elastic or plastic, or hard. In total, six sets of samples were tested from 0wt% to 15wt%.

Table 4.3

Tensile Test Results

MWCNT-PDMS Film with Different Concentration	Maximum Average Force (N)	Maximum Average Stress (MPa)	Maximum Displacement (mm)	Elastic Modulus (MPa)
0wt%	8.54	1.71	34.25	1.01
0.1wt%	4.42	0.88	36.94	1.2
1wt%	6.96	1.39	37.31	1.87
10wt%	11.35	2.27	31.96	2.38
12wt%	12.94	2.59	25.71	5.51
15wt%	13.81	2.76	22.19	6.95

The length and the area of the films are identical, where the elastic modulus depends on the maximum force and the maximum displacement of the films. From PDMS to 0.1 wt% and later to 1 wt% MWCNT-PDMS film, the maximum force, as well as the maximum force, were increasing gradually, which also made the elastic modulus increase in a sort range. When the concentration was upgraded to 10 wt%, 12 wt% and 15 wt%, the maximum force increased dramatically while the maximum displacement started decreasing. This indicates that although the elastic modulus was rising, due to

the increased hardness for the higher amount of MWCNT powder, higher force was required even to pull out less displacement.

Figure 4.7

Stress vs Strain Curve of (a) PDMS (0wt%) (b) 0.1 wt% (c) 1 wt% (d) 10 wt% (e) 12 wt% (f) 15 wt% Films

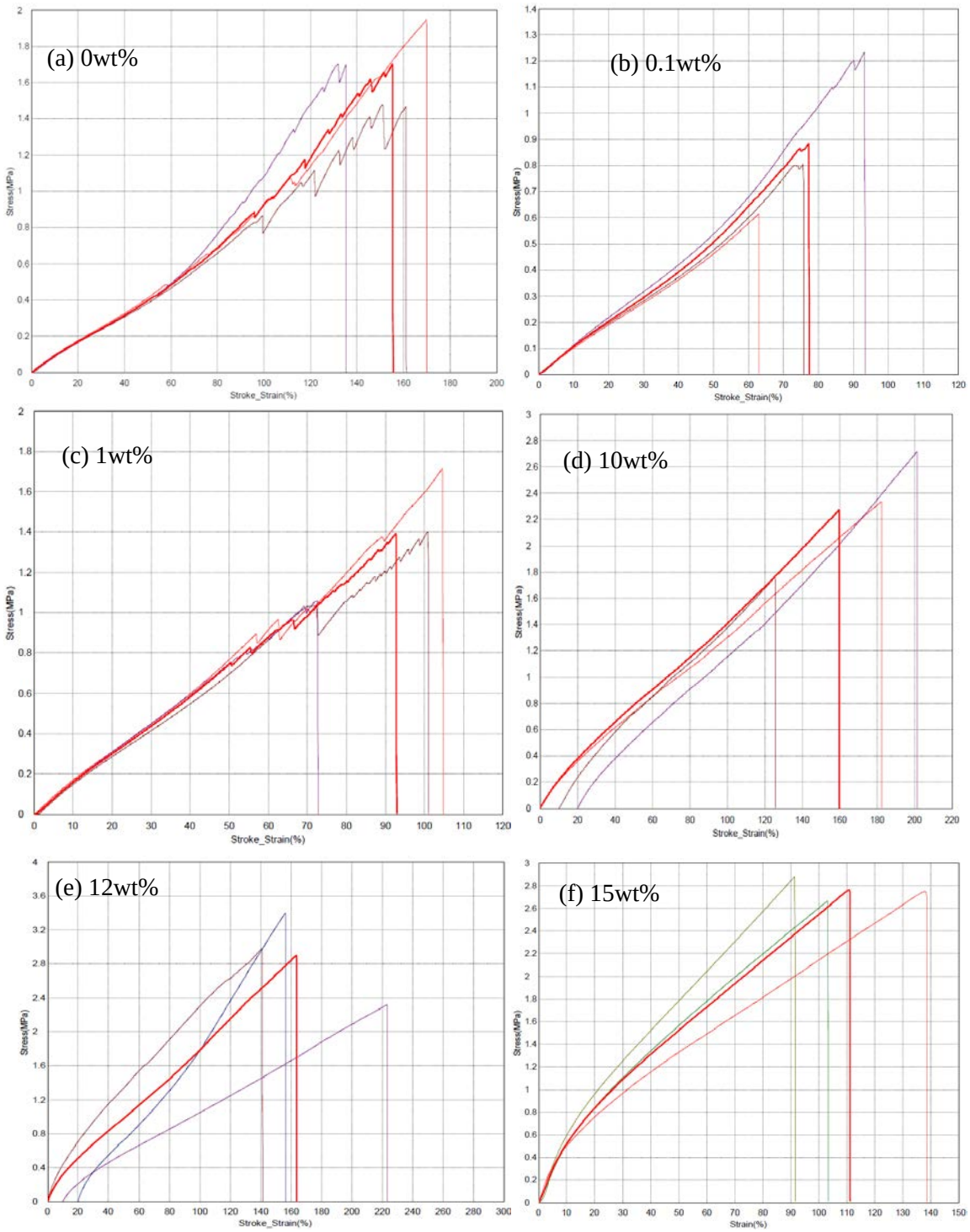

As a higher concentration of CNT was making the film harder and affecting the flexibility of the film, the 10 wt% and 12 wt% MWCNT-PDMS films were selected for the system since still, they were making a sufficient amount of maximum displacement within a similar maximum force to 15 wt% MWCNT-PDMS film. The bold red line represents the average stress vs strain curve in each graph.

4.3.4 Electro-Mechanical Characteristics of the Films

The MWCNT-PDMS film, due to being very elastic or flexible, provided changes in current for a very small change in the distance between the electrodes for different bends. The voltage was fixed to 3 V, and changes in current due to different bends were recorded. It was observed that due to the increase in the bending, the current was decreasing since the bending in the film was making the electrodes get apart in a longer gap than the gap with no bending. Due to the increased gap, the resistance of the film increased, and the current was increased as the resistance and current are inversely proportional. The change in current for 0° to 3° was observed, and the same process was repeated for ten cycles where similar outcomes came out. The current was decreasing with a very little bending almost linearly with a sensitivity of 0.43 kΩ/° (Figure 4.8 (a)). It can be beneficial to measure the current changes with a few bending due to the low flow rate. In general, the sensor showed the change in current instantly with the bending where it took on an average of 15 minutes to go back to its initial current with 0° bending (Figure 4.8 (b)).

Table 4.4

Electromechanical Characterization Data

Bending Angle (θ°)	$R_{average}$ (kΩ)
0	2.93 ± 0.01
0.5	3.16 ± 0.04
1	3.39 ± 0.08
1.5	3.57 ± 0.09
2	3.78 ± 0.08
2.5	3.97 ± 0.11
3	4.28 ± 0.17

Figure 4.8

(a) Average Resistance vs the Bending Angle (b) Response of the Sensor in Each Cycle

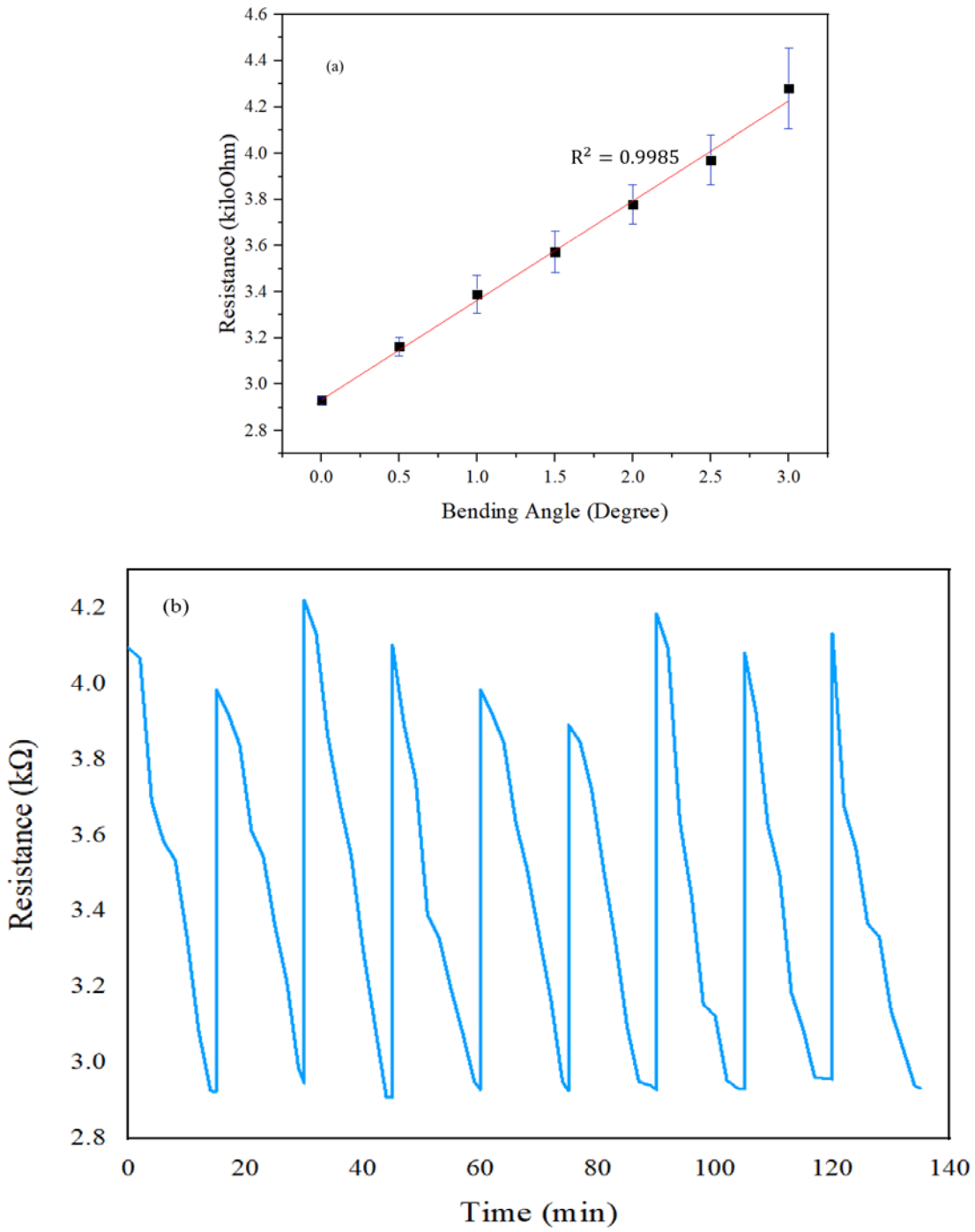

The hysteresis diagrams for each cycle were plotted, and from those, it was observed that in each cycle, there is a path gap in-between the response and recovery of the sensor (Figure 4.9). The hysteresis graphs were analyzed for individual cycles that were observed. Since the response time and the recovery time for each cycle are not similar, the number of observations during the response and the recovery period was considered

to plot the hysteresis curves. It was found that in most of these cycles, there was a hysteresis loop which means the recovery did not happen like the response of the change in the film resistance.

Figure 4.9

Hysteresis for Each cycle

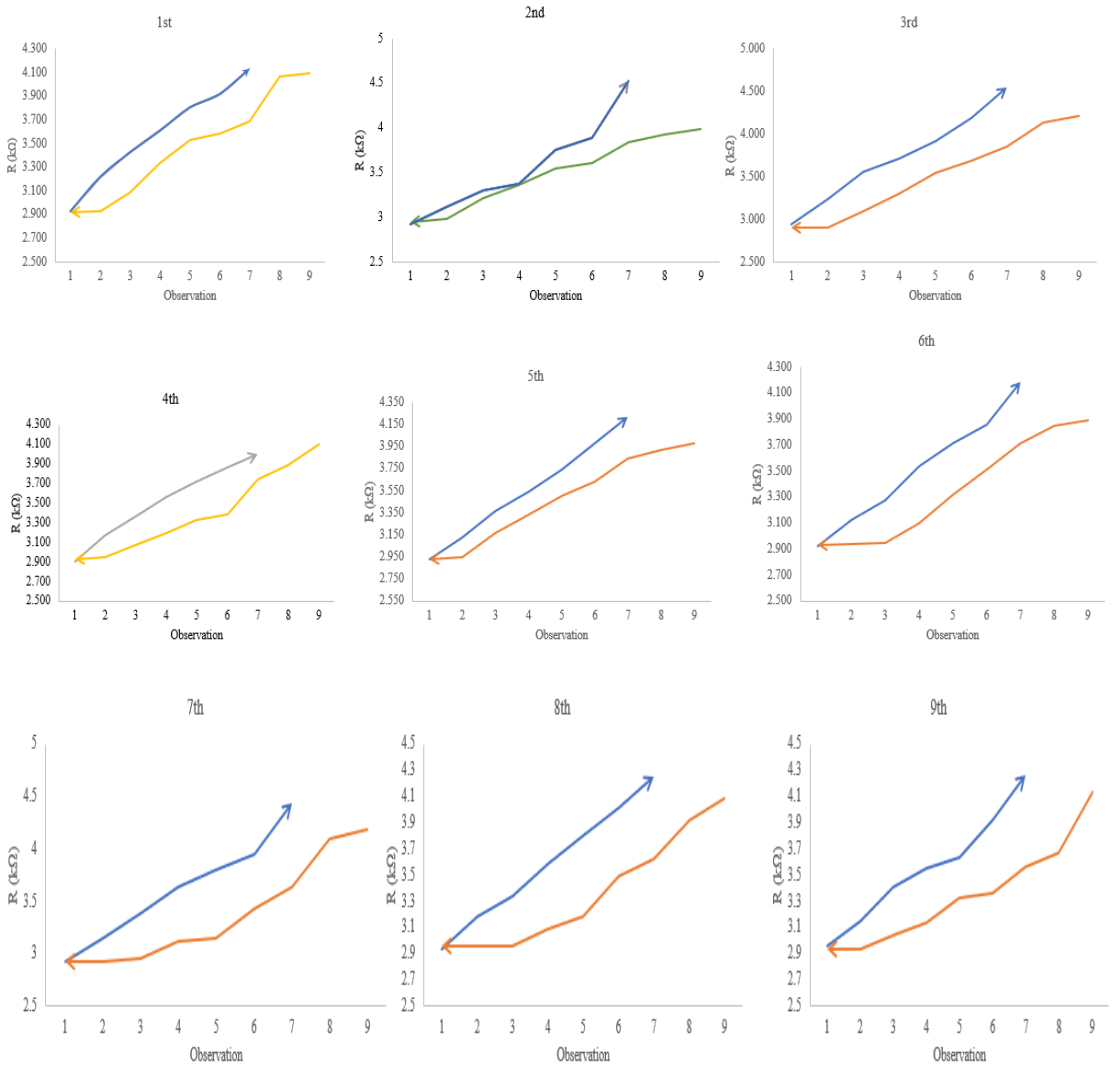

4.4 Flow Sensor Fabrication and Performance Evaluation

4.4.1 Flow Rate Detection

The sensor was characterized with six different flow rates which are 0 µL/s, 50 µL/s, 100 µL/s, 150 µL/s, 200 µL/s and 250 µL/s. Furthermore, the sensor behaviour for these flow rates was observed for three different flow channels with diameters of 3 mm, 5 mm and 7 mm. Firstly, the system with a 5 mm diameter was experimented with these

six different flow rates. Depending on the channel diameter and flow rate, the pressure change, head loss, Reynolds number as well as friction coefficient varied. The value of Reynolds number (R_e) less than 2300 indicates the behavior of the flow is 'laminar' where the value of R_e within 2300 and 4000 indicates 'transitional' flow and if the value of R_e is greater than 4000 indicates 'turbulent' flow (Yunus 2010).

Table 4.5

Fluid Flow Parameters for the Different Channel Diameter of 3 mm, 5 mm and 7 mm

Diameter = 3 mm						
Flow Rate (μL/s)	Velocity (m/s)	Reynold's Number	Flow Type	Friction Factor, f	Head Loss (m)	P_L (Nm^{-2})
0	0.0000	0	Laminar	N/A	N/A	N/A
50	0.0071	23.7719	Laminar	2.692	0.000115	1.119
100	0.0141	47.5438	Laminar	1.346	0.000229	2.238
150	0.0212	71.3157	Laminar	0.897	0.000344	3.358
200	0.0283	95.0876	Laminar	0.673	0.000458	4.477
250	0.0354	118.859	Laminar	0.538	0.000573	5.596
Diameter = 5 mm						
Flow Rate (μL/s)	Velocity (m/s)	Reynold's Number	Flow Type	Friction Factor, f	Head Loss (m)	P_L (Nm^{-2})
0	0.0000	0	Laminar	N/A	N/A	N/A
50	0.003	14.26	Laminar	4.487	1.48E-05	0.145
100	0.005	28.53	Laminar	2.244	2.97E-05	0.290
150	0.008	42.79	Laminar	1.496	4.45E-05	0.435
200	0.010	57.05	Laminar	1.122	5.94E-05	0.580
250	0.013	71.32	Laminar	0.897	7.42E-05	0.725
Diameter = 7 mm						
Flow Rate (μL/s)	Velocity (m/s)	Reynold's Number	Flow Type	Friction Factor, f	Head Loss (m)	P_L (Nm^{-2})
0	0.0000	0.00	Laminar	N/A	N/A	N/A
50	0.0013	10.19	Laminar	6.282	3.86E-06	0.038
100	0.0026	20.38	Laminar	3.141	7.73E-06	0.076
150	0.0039	30.56	Laminar	2.094	1.16E-05	0.113
200	0.0052	40.75	Laminar	1.570	1.55E-05	0.151
250	0.0065	50.94	Laminar	1.256	1.93E-05	0.189

From Table 4.5, it is illustrated that for each channel diameter, the velocity and the Reynold number increased with the increase in the flow rate, although these two

parameters in each flow rates were comparatively less while increasing the diameter of the channel. The value of R_e less than 2300 indicates the flows are laminar types. The head loss is very negligible in every case. The pressure drop increased with the increase in the flow, which indicates that the pressure, as well as the force on the sensor, decreases with the increase in the flow rate. However, this pressure drop is very negligible for 5 mm channel. Therefore, the sensor can be placed anywhere inside the channel except at the inlet point of the channel just to avoid the fluctuation due to the direct hit of the flow on the sensor. Otherwise, there may have some fluctuation in the data while recording the performance

4.4.2 Reference Sensor and Testing Sensor Characteristics

The resistances for the reference sensor and testing sensor were recorded for 90 minutes. In the case of the reference sensor, the current kept on decreasing gradually with time; however, the drop of current is comparatively slower than the drop of current in the testing sensor. For testing sensor, the change or rise in resistance was noticed generally after 20 s or mostly 25 s. Later, the resistance fixed to that value with some fluctuation for the rest of the time. This is one of the observations among seven sets of observations. Figure 4.10 demonstrates that the resistance of the reference sensor increased with time almost linearly with a very small change compared to the change in resistance there is a flow in the testing sensor.

Figure 4.10

Current vs Time Graphs for Different Flow Rates

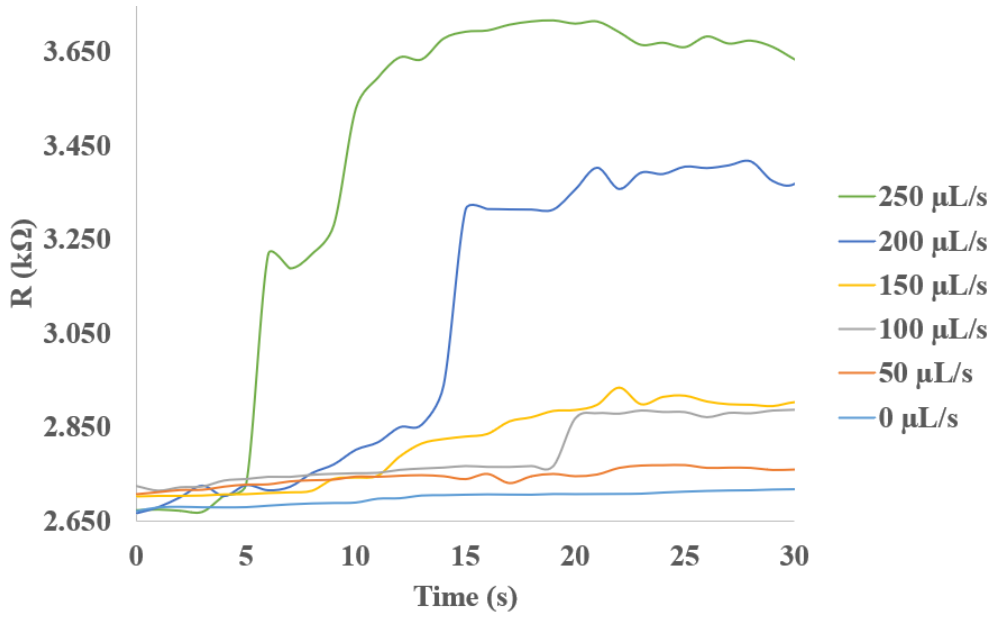

In the case of 50 µL/s, the change in resistance after 20 s is almost similar to the reference sensor, which is 43 Ω. The change in resistance in the case of 100 µL/s after 20 s is still very small, which is 194 Ω. Significant changes in current were observed at 150 µL/s, 200 µL/s and 250 µL/s which are 266 Ω, 667 Ω and 972 Ω respectively. These changes were noticed mostly after 20 s, and after the rest of the time, the resistances were almost fixed at their respective values for the rest of the time, which was observed until 90 s. The average of the change in resistance after 20 s due to different flow rates were calculated and plotted against the flow rates. It was found that for smaller flow rate, e.g. 0 µL/s and 50 µL/s, there was almost no change in current rather, it behaved like the reference sensor. When there was a flow of 100 µL/s, and 150 µL/s, the average change in resistance was found 95.04 Ω and 203.66 Ω respectively. However, with higher flow rates such as 200 µL/s and 250 µL/s, the testing sensor showed quite a significant average resistance change which are 637.47 Ω and 948.6 Ω, respectively. Although in the case of lower flow rates such as 100 µL/s and 150 µL/s, the standard deviation is a little high, it decreases as the flow rate increases. It indicates that the sensor is not appropriately sensitive towards a lower flow rate. However, the system did not show proper consistency in its data.

Figure 4.11

Average Resistance Change vs Flow Rate for 5 mm Channel

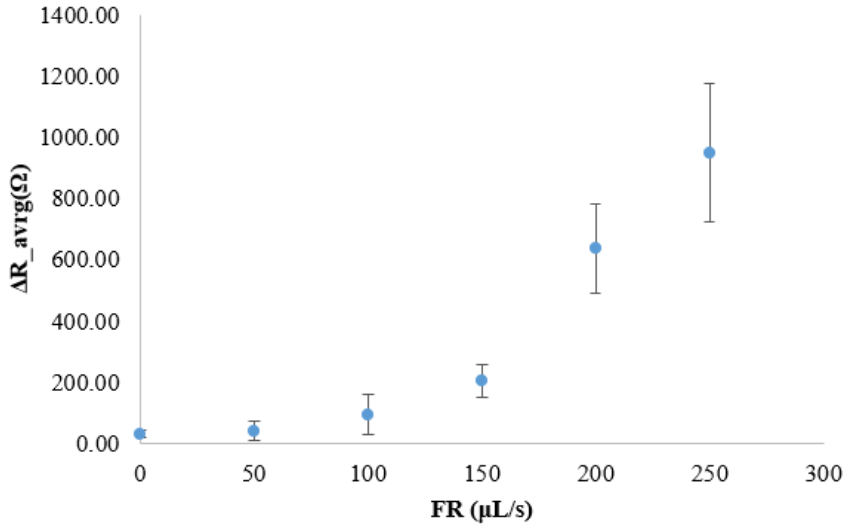

The sensor was tested for different flow rates simultaneously. Initially, for no flow rate, the resistance was 2.55 kΩ. When 50 µL/s was provided through the channel, there was no significant change observed, a very negligible change for 100 µL/s and 150 µL/s respectively—however, significance in resistance change with a value of 612 Ω and 1160 Ω, respectively. Later, the flow rate was stopped, and it was found that the system took almost 5 minutes to get recovered. In Figure 4.12, the ratio of the average change in resistance of the testing sensor and reference sensor was plotted against different flow rates. The changes in resistance were observed in the 20s after the water started flowing through the flow channel; for 0 µL/s flow rate, the ratio was one since there was no difference between the testing sensor and the reference sensor. However, as the flow rate was increased, the changes of resistance in the testing sensor became higher than the change of resistance in the reference sensor after the 20s. Because for higher flow rates of water, a comparatively higher amount of force was implied on the film, which resulted in higher bending as well as the higher gap between the electrodes. Therefore, although the change in reference resistance was fixed, the change in testing resistance varied for different flow rates, which provided a higher value of this ratio for higher flow rates. Moreover, for higher flow rates of water, the standard deviation was observed larger than the standard deviation for lower flow rates.

Figure 4.12

The Ratio of Average Change in Resistance for Testing Sensor and Reference Sensor within the 20s vs Flow Rates of Water

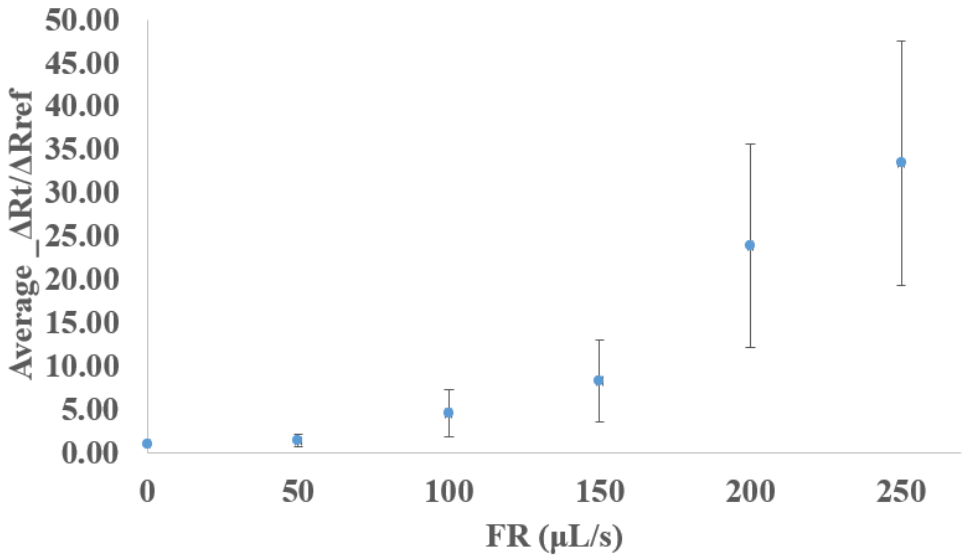

The flow rates have also been experimented with for the channel diameter of 3 mm and 7 mm. It was observed that in the case of the 3 mm channel, the testing sensor behaved like the reference sensor. Because the sensor film was almost stuck inside the channel as the width of the film is almost the same as the channel, which is 3.5 mm approximately. On the other hand, the 7 mm channel showed some different characteristics in terms of the flow rates. For bigger diameter, the pressure became smaller, although the dimension of the film was the same. There were almost no significant changes due to the flow rates up to 200 µL/s; rather, the test sensor behaved like the reference sensor. However, some changes due to the flow rates for 250 µL/s was observed. The LOD was found 38.55 Ω, which indicates that a minimum 250 µL/s flow rate can be measured using the 7 mm channel.

Figure 4.13

Average Current Change vs Flow Rate for 7 mm Channel

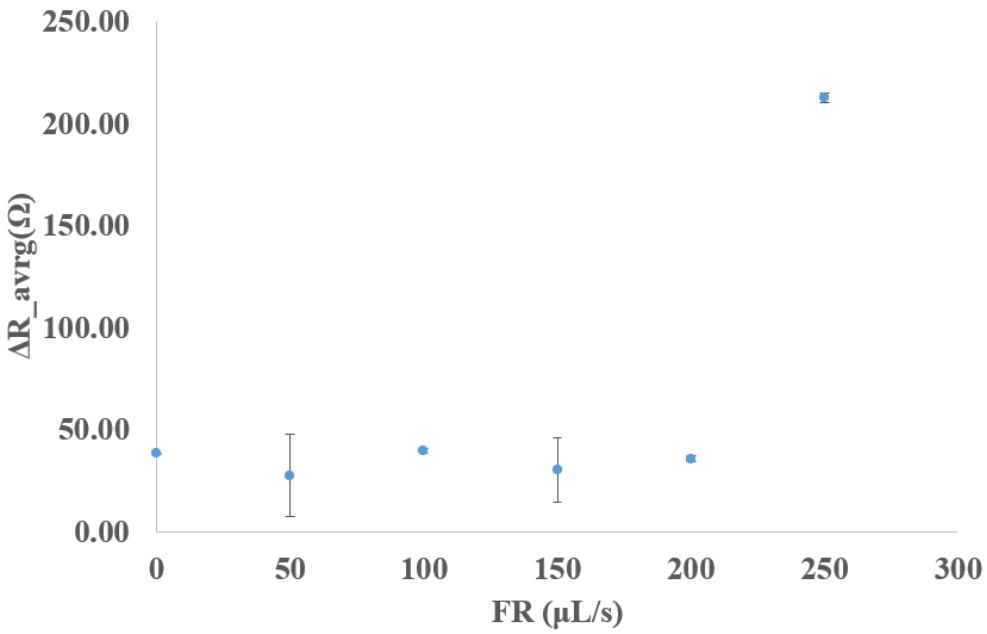

4.4.3 Limit of Detection (LOD)

The LOD of the system is 35.64 Ω with the numerical factor 2. Table 4.6 shows that the flow rate below 100 µL/s deals with currently less than the LOD, which means the system is not able to detect the flow rates less than 100 µL/s. However, for 100 µL/s and above, the currents are higher than LOD that indicates that the system is sensitive or responsive for flow rates above 100 µL/s.

Table 4.6

Limit of Detection (LOD) for 5 mm Channel

FR (µL/s)	ΔR_avrg(Ω)	LOD (Ω)	(+ve)	(-ve)
0	31.64	35.64	44.30	18.98
50	41.82		73.69	9.95
100	95.04		159.06	31.02
150	203.66		256.89	150.42
200	637.47		784.33	490.61
277	948.60		1174.18	723.02

4.4.4 Response and Recovery

The response time and the recovery time of the sensor were recorded for ten cycles. In Figure 4.15, it can be seen that initially, when there is no flow, the resistance was fixed to almost 2.641 Ω for 1 minute. When there is a flow, the resistance increased when there was flow within 20 s and later, when the flow is stopped, it started decreasing as the sensor started recovering its initial straight position from bending position. It took most, on average, 5 minutes to get recovered from its bending state to the initial state in each cycle.

Figure 4.14

Simultaneous Response for Different Flow Rates and Recovery Times of the System

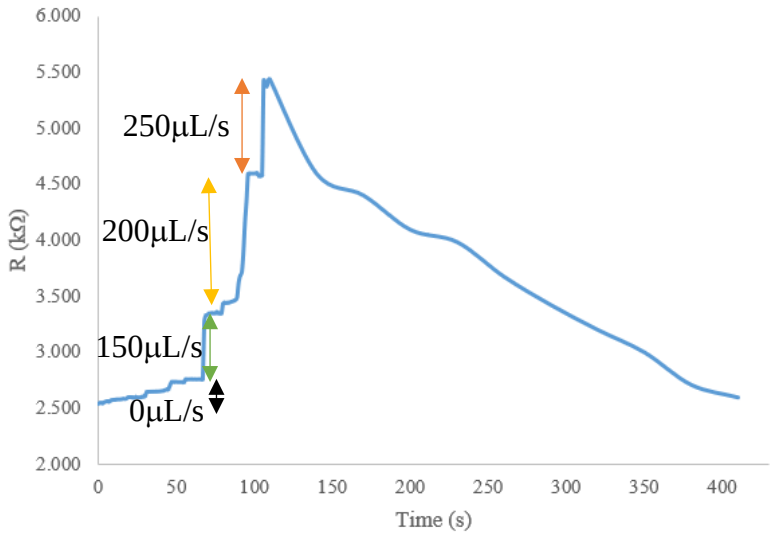

Figure 4.15

Response and Recovery Cycle of the Sensor

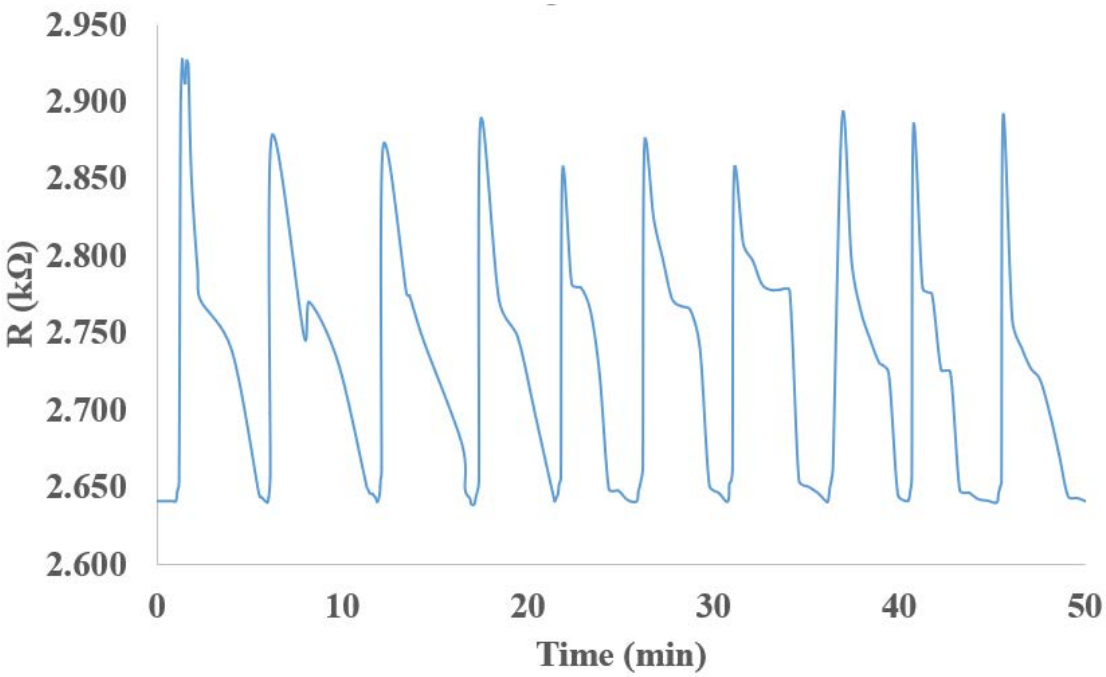

CHAPTER 5
CONCLUSION AND RECOMMENDATIONS

5.1 Conclusion

The Electrically conducting MWCNT-PDMS nanocomposite was successfully prepared where the concentration of MWCNT in the PDMS matrix was varied between 1 to 20 wt%. Up to 5 wt% MWCNT concentrations, the MWCNT-PDMS nanocomposite did not show any electrical conductivity. From 8 wt% MWCNT concentration and onwards, electrical conductivity was observed in the MWCNT-PDMS nanocomposite, which was found to increase gradually with increasing MWCNT concentrations. At 12 wt% MWCNT concentration, the MWCNT-PDMS film exhibited 2.55 kΩ electrical resistance. However, an inhomogeneous mixture was observed above 12 wt% MWCNT concentrations making it difficult to obtain a thin-film structure.

Upon addition of MWCNT, the surface wettability of the MWCNT-PDMS thin film became more hydrophobic. For plain PDMS thin film, an average water contact angle of 107.50° was recorded, which then gradually increased with MWCNT concentration, reaching a value up to 128.57° at 12 wt% MWCNT in the PDMS matrix. The elastic modulus of the MWCNT-PDMS film was also found to increase with increasing MWCNT concentration indicating that the addition of MWCNT makes PDMS film more resistant to deformation when stress is applied to the film. The study on the electro-mechanical properties of the 12 wt% MWCNT-PDMS film revealed that the electrical resistance of the film increases with applied bending on the film. The film's electrical resistance exhibited a linear response against the applied bending with a sensitivity of 0.43 kΩ/° and showed good reproducibility.

A flow rate sensor was then successfully designed and fabricated by using the 12 wt% MWCNT-PDMS film as the main sensing element. The sensor performance was tested for different water flow rate ranging from 0 to 250 µl/s. At different flow rates, the fabricated sensor showed variations in its electrical resistance, where the electrical resistance of the MWCNT-PDMS film was found to have a direct relationship with the flow rate of the liquid. With the increasing flow rate of the water, the sensor electrical resistance was observed to increase, demonstrating a good response time of ~20 s. The

fabricated MWCNT-PDMS sensor showed a limit of detection (LoD) equal to 150 µl/s, which is comparable to several commercially available flow rate sensors. The results from this study showed promise towards an affordable and simple liquid flow rate sensor, and by careful control on the sensor design, it is possible to lower the LoD of the sensor further, making it potential for biomedical applications.

5.2 Recommendations for Future Studies

This research can be further improvised by taking care of the following factors mentioned as recommendations:

1. The spreading of the mixture of MWCNT and PDMS for higher concentration was hard since it was necessary to maintain the homogeneous thickness of the film. Therefore, a better option for mold preparation as well as the spreading method can be developed.
2. Thinner aluminium electrodes were desired to get the better bend in the film. However, due to the hardship to spread the high concentrated MWCNT-PDMS mixture, it was not possible to use too much thin (e.g. one layer of aluminium foil) electrodes. A better and thinner option of electrodes can be taken under consideration.
3. A smaller diameter of the channel can be achieved by making the sensor width smaller. Since the width of the film was already larger than 3 mm, it could not get fitted into the 3 mm or less channel diameter for bending; rather, the sensor was stuck into the channel.
4. The detection limit of the flow rate can be improved, and also different conductive and nonconductive liquids with various viscosity can be used to characterize the system performance.
5. The sensor film should not be made extremely thin (e.g. less than 0.5 mm) since it may not get recovered after once it gets bent due to the flow rates.
6. As the system lacks consistency in its performance, a better mechanism to record the system parameters, such as resistance changes, pressure on the film, bending mechanism etc., can be improved.

REFERENCES

Alveringh, D., Sanders, R. G., Wiegerink, R. J., & Lötters, J. C. (2016). *Vortex generation and sensing in microfabricated surface channels.* Paper presented at the 2016 IEEE 29th International Conference on Micro Electro Mechanical Systems (MEMS).

Alveringh, D., Wiegerink, R. J., Groenesteijn, J., Sanders, R. G., & Lötters, J. C. (2018). Experimental analysis of thermomechanical noise in micro Coriolis mass flow sensors. *Sensors and actuators A: Physical, 271*, 212-216.

Alveringh, D., Wiegerink, R. J., & Lötters, J. C. (2017). Integrated pressure sensing using capacitive Coriolis mass flow sensors. *Journal of microelectromechanical systems, 26*(3), 653-661.

Angarita-Jaimes, N., McGhee, E., Chennaoui, M., Campbell, H., Zhang, S., Towers, C., . . . Towers, D. (2006). Wavefront sensing for single view three-component three-dimensional flow velocimetry. *Experiments in fluids, 41*(6), 881-891.

Antony, R., Nandagopal, M. G., Sreekumar, N., & Selvaraju, N. (2014). Detection principles and development of microfluidic sensors in the last decade. *Microsystem technologies, 20*(6), 1051-1061.

Baek, S. H., Roh, J., Park, C. Y., Kim, M. W., Shi, R., Kailasa, S. K., & Park, T. J. (2020). Cu-nanoflower decorated gold nanoparticles-graphene oxide nanofiber as electrochemical biosensor for glucose detection. *Materials Science and Engineering: C, 107*, 110273.

Baker, R. C. (1994). Coriolis flowmeters: industrial practice and published information. *Flow Measurement and Instrumentation, 5*(4), 229-246.

Baldwin, A., Hudson, T., & Meng, E. (2018). *A calorimetric flow sensor for ultra-low flow applications using electrochemical impedance.* Paper presented at the 2018 IEEE Micro Electro Mechanical Systems (MEMS).

Bandura, D. R., Baranov, V. I., Ornatsky, O. I., Antonov, A., Kinach, R., Lou, X., . . . Tanner, S. D. (2009). Mass cytometry: technique for real time single cell multitarget immunoassay based on inductively coupled plasma time-of-flight mass spectrometry. *Analytical chemistry, 81*(16), 6813-6822.

Berthet, H., Jundt, J., Durivault, J., Mercier, B., & Angelescu, D. (2011). Time-of-flight thermal flowrate sensor for lab-on-chip applications. *Lab on a Chip, 11*(2), 215-223.

Chen, J., Li, X., Edmondson, A., Meyers, G. D., Izumi, K., Ackermann, A. M., . . . He, M. (2019). Increased Clinical Sensitivity and Specificity of Plasma Protein N-Glycan Profiling for Diagnosing Congenital Disorders of Glycosylation by Use of Flow Injection–Electrospray Ionization–Quadrupole Time-of-Flight Mass Spectrometry. *Clinical chemistry, 65*(5), 653-663.

Chen, J., Zhou, Y., Wang, D., He, F., Rotello, V. M., Carter, K. R., . . . Nugen, S. R. (2015). UV-nanoimprint lithography as a tool to develop flexible microfluidic devices for electrochemical detection. *Lab on a Chip, 15*(14), 3086-3094.

Chen, Y. J., Schoeler, U., Huang, C. H., & Vollmer, F. (2018). Combining Whispering-Gallery Mode Optical Biosensors with Microfluidics for Real-Time Detection of Protein Secretion from Living Cells in Complex Media. *Small, 14*(22), 1703705.

Cheri, M. S., Latifi, H., Sadeghi, J., Moghaddam, M. S., Shahraki, H., & Hajghassem, H. (2014). Real-time measurement of flow rate in microfluidic devices using a cantilever-based optofluidic sensor. *Analyst, 139*(2), 431-438.

Chung, K., Lee, H., & Lu, H. (2009). Multiplex pressure measurement in microsystems using volume displacement of particle suspensions. *Lab on a Chip, 9*(23), 3345-3353.

Chung, W. (2019). Liquid Flowmeter Using Thermal Measurement; Design and Application.

Cierpka, C., & Kähler, C. (2012). Particle imaging techniques for volumetric three-component (3D3C) velocity measurements in microfluidics. *Journal of visualization, 15*(1), 1-31.

Cooper, K., Pickrell, G., & Wang, A. (2003). Optical Fiber Sensor Technologies for Efficient and Economical Oil Recovery: Virginia Polytechnic Institute and State University (US).

Davaji, B. (2016). Thermal Microfluidic Devices; Design, Fabrication and Applications.

Davaji, B., Jeong Bak, H., Chang, W.-J., & Hoon Lee, C. (2014). A novel on-chip three-dimensional micromachined calorimeter with fully enclosed and suspended thin-film chamber for thermal characterization of liquid samples. *Biomicrofluidics, 8*(3), 034101.

Eivazzadeh-Keihan, R., Pashazadeh, P., Hejazi, M., de la Guardia, M., & Mokhtarzadeh, A. (2017). Recent advances in nanomaterial-mediated bio and immune sensors for detection of aflatoxin in food products. *TrAC Trends in Analytical Chemistry, 87*, 112-128.

Fallahi, H., Zhang, J., Phan, H.-P., & Nguyen, N.-T. (2019). Flexible microfluidics: fundamentals, recent developments, and applications. *Micromachines, 10*(12), 830.

Ghazavi, M., & Molki, H. (2017). Nonlinear vibration and stability analysis of the curved microtube conveying fluid as a model of the micro coriolis flowmeters based on strain gradient theory. *Applied Mathematical Modelling, 45*, 1020-1030.

Ghommem, M., Calo, V. M., & Claudel, C. G. (2015). Micro-cantilever flow sensor for small aircraft. *Journal of Vibration and Control, 21*(10), 2043-2058.

Gnyawali, V., Strohm, E. M., Wang, J.-Z., Tsai, S. S., & Kolios, M. C. (2019). Simultaneous acoustic and photoacoustic microfluidic flow cytometry for label-free analysis. *Scientific reports, 9*(1), 1-11.

Grandchamp, X., Van Hirtum, A., & Pelorson, X. (2010). Hot film/wire calibration for low to moderate flow velocities. *Measurement Science and Technology, 21*(11), 115402.

Groenesteijn, J., de Boer, M. J., Lötters, J. C., & Wiegerink, R. J. (2017). A versatile technology platform for microfluidic handling systems, part I: fabrication and functionalization. *Microfluidics and nanofluidics, 21*(7), 127.

Groenesteijn, J., Sanders, R. G., Wiegerink, R. J., & Lötters, J. C. (2016). *Towards nanogram per second coriolis mass flow sensing.* Paper presented at the 2016 IEEE 29th International Conference on Micro Electro Mechanical Systems (MEMS).

Hallam, J. M., Rigas, E., Charrett, T. O., & Tatam, R. P. (2020). 2D Spatially-Resolved Depth-Section Microfluidic Flow Velocimetry Using Dual Beam OCT. *Micromachines, 11*(4), 351.

Haneveld, J., Lammerink, T. S., de Boer, M. J., Sanders, R. G., Mehendale, A., Lötters, J. C., . . . Wiegerink, R. (2010). Modeling, design, fabrication and characterization of a micro Coriolis mass flow sensor. *Journal of micromechanics and microengineering, 20*(12), 125001.

Haneveld, J., Lammerink, T. S., de Boer, M. J., & Wiegerink, R. J. (2009). *Micro Coriolis mass flow sensor with integrated capacitive readout.* Paper presented at the 2009 IEEE 22nd International Conference on Micro Electro Mechanical Systems.

Haneveld, J., Lammerink, T. S., Dijkstra, M., Droogendijk, H., de Boer, M. J., & Wiegerink, R. J. (2008). *Highly sensitive micro coriolis mass flow sensor.* Paper presented at the 2008 IEEE 21st International Conference on Micro Electro Mechanical Systems.

Harel, E., Hilty, C., Koen, K., McDonnell, E. E., & Pines, A. (2007). Time-of-flight flow imaging of two-component flow inside a microfluidic chip. *Physical review letters, 98*(1), 017601.

He, Y., Ming, Y., Li, W., Li, Y., Wu, M., Song, J., . . . Liu, H. (2018). Highly stable and flexible pressure sensors with modified multi-walled carbon nanotube/polymer composites for human monitoring. *Sensors, 18*(5), 1338.

Henderson, D. A. (2007). Novel piezo motor enables positive displacement microfluidic pump. *Stroke (mm), 50*, 10.

Hennemeyer, M., Burghardt, S., & Stark, R. W. (2008). Cantilever micro-rheometer for the characterization of sugar solutions. *Sensors, 8*(1), 10-22.

Hoera, C., Kiontke, A., Pahl, M., & Belder, D. (2018). A chip-integrated optical microfluidic pressure sensor. *Sensors and Actuators B: Chemical, 255*, 2407-2415.

Hogendoorn, J., Hofstede, H., van Brakel, P., & Boer, A. (2011). *How accurate are ultrasonic flowmeters in practical conditions; beyond the calibration.* Paper presented at the 29th International North Sea Flow Measurement Workshop, 25.-28. October 2011, Tonsberg, Norway.

Huber, C. (2016). MEMS-based Micro-Coriolis Density and Flow Measurement Technology. *tm-Technisches Messen, 83*(3), 157-162.

Jang, H., Yoon, H., Ko, Y., Choi, J., Lee, S.-S., Jeon, I., . . . Kim, H. (2016). Enhanced performance in capacitive force sensors using carbon nanotube/polydimethylsiloxane nanocomposites with high dielectric properties. *Nanoscale, 8*(10), 5667-5675.

Jeong, S., Park, J., Pathania, D., Castro, C. M., Weissleder, R., & Lee, H. (2016). Integrated magneto–electrochemical sensor for exosome analysis. *ACS nano, 10*(2), 1802-1809.

King, L. V. (1914). XII. On the convection of heat from small cylinders in a stream of fluid: Determination of the convection constants of small platinum wires with applications to hot-wire anemometry. *Philosophical transactions of the royal society of London. series A, containing papers of a mathematical or physical character, 214*(509-522), 373-432.

Kit, E., & Liberzon, D. (2016). 3D-calibration of three-and four-sensor hot-film probes based on collocated sonic using neural networks. *Measurement Science and Technology, 27*(9), 095901.

Kitsos, V., Demosthenous, A., & Liu, X. (2019). A smart dual-mode calorimetric flow sensor. *IEEE Sensors Journal, 20*(3), 1499-1508.

Kuo, J. T., Chang, L.-Y., Li, P.-Y., Hoang, T., & Meng, E. (2011). A microfluidic platform with integrated flow sensing for focal chemical stimulation of cells and tissue. *Sensors and Actuators B: Chemical, 152*(2), 267-276.

Kuo, J. T., Yu, L., & Meng, E. (2012). Micromachined thermal flow sensors—A review. *Micromachines, 3*(3), 550-573.

Lake, J. R., Heyde, K. C., & Ruder, W. C. (2017). Low-cost feedback-controlled syringe pressure pumps for microfluidics applications. *PLoS One*, *12*(4), e0175089.

Lammerink, T. S., Lötters, J. C., Wiegerink, R. J., Groenesteijn, J., & Haneveld, J. (2011). *Single chip flow sensing system with a dynamic flow range of more than 4 decades.* Paper presented at the 2011 16th International Solid-State Sensors, Actuators and Microsystems Conference.

Lang, H. P., & Gerber, C. (2008). Microcantilever sensors *STM and AFM studies on (bio) molecular systems: unravelling the nanoworld* (pp. 1-27): Springer.

Lee, S. H., & Kang, P. K. (2020). Three-Dimensional Vortex-Induced Reaction Hot Spots at Flow Intersections. *Physical review letters*, *124*(14), 144501.

Leitgeb, R. A., Werkmeister, R. M., Blatter, C., & Schmetterer, L. (2014). Doppler optical coherence tomography. *Progress in retinal and eye research*, *41*, 26-43.

Li, Y., Lu, Y., Xie, B., Chen, J., Wang, J., & Chen, D. (2020). A Micromachined Resonant Differential Pressure Sensor. *IEEE Transactions on Electron Devices*, *67*(2), 640-645.

Li, Y., Yan, G., Zhang, L., & He, S. (2015). Microfluidic flowmeter based on micro "hot-wire" sandwiched Fabry-Perot interferometer. *Optics Express*, *23*(7), 9483-9493.

Lima, R., Wada, S., Takeda, M., Tsubota, K.-i., & Yamaguchi, T. (2007). In vitro confocal micro-PIV measurements of blood flow in a square microchannel: the effect of the haematocrit on instantaneous velocity profiles. *Journal of biomechanics*, *40*(12), 2752-2757.

Luo, J., Fu, Y. Q., & Milne, W. (2013). Acoustic wave based microfluidic and lab-on-chip.

Lyu, G., Che, G., Li, J., Jiang, X., Wang, K., Han, Y., & Gao, L. (2017). Design of novel FBG-based sensor of differential pressure with magnetic transfer. *Sensors*, *17*(2), 375.

Mark, D., Haeberle, S., Roth, G., Von Stetten, F., & Zengerle, R. (2010). Microfluidic lab-on-a-chip platforms: requirements, characteristics and applications *Microfluidics based microsystems* (pp. 305-376): Springer.

Martin, S., & Bhushan, B. (2017). Transparent, wear-resistant, superhydrophobic and superoleophobic poly (dimethylsiloxane)(PDMS) surfaces. *Journal of colloid and interface science*, *488*, 118-126.

Mi, S., Pu, H., Xia, S., & Sun, W. (2020). A Minimized Valveless Electromagnetic Micropump for Microfluidic Actuation on Organ Chips. *Sensors and actuators A: Physical*, *301*, 111704.

Microfluidic low-flow liquid flow meter: a review, Elveflow, 2020. (2020). from https://www.elveflow.com/microfluidic-reviews/microfluidic-flow-control/microfluidic-low-flow-liquid-flow-meters-a-review/

Mohd, O., Sotoudegan, M. S., Ligler, F. S., & Walker, G. M. (2019). A simple cantilever system for measurement of flow rates in paper microfluidic devices. *Engineering Research Express*, *1*(2), 025019.

Noeth, N., Keller, S. S., & Boisen, A. (2014). Integrated cantilever-based flow sensors with tunable sensitivity for in-line monitoring of flow fluctuations in microfluidic systems. *Sensors*, *14*(1), 229-244.

O'Donovan, T. S., Persoons, T., & Murray, D. B. (2011). High-resolution hot-film measurement of surface heat flux to an impinging jet. *Measurement Science and Technology*, *22*(10), 105402.

Orth, A., Schonbrun, E., & Crozier, K. B. (2011). Multiplexed pressure sensing with elastomer membranes. *Lab on a Chip, 11*(22), 3810-3815.

Peng, J., Fu, X., & Chen, Y. (2004). Flow measurement by a new type vortex flowmeter of dual triangulate bluff body. *Sensors and actuators A: Physical, 115*(1), 53-59.

Pradeep, A., Stanley, J., Nair, B. G., & Babu, T. S. (2018). Automated and programmable electromagnetically actuated valves for microfluidic applications. *Sensors and actuators A: Physical, 283*, 79-86.

Prasad, R., Kumar, M., & Kumar, V. (2017). *Nanotechnology: an agricultural paradigm*: Springer.

Ramalingame, R., Lakshmanan, A., Müller, F., Thomas, U., & Kanoun, O. (2019). Highly sensitive capacitive pressure sensors for robotic applications based on carbon nanotubes and PDMS polymer nanocomposite. *Journal of Sensors and Sensor Systems, 8*(1), 87-94.

Ramalingame, R., Udhayakumar, N., Torres, R., Neckel, I., Müller, C., & Kanoun, O. (2016). MWCNT-PDMS nanocomposite based flexible multifunctional sensor for health monitoring. *Procedia Engineering, 168*, 1775-1778.

Rubenstein, D., Yin, W., & Frame, M. D. (2015). *Biofluid mechanics: an introduction to fluid mechanics, macrocirculation, and microcirculation*: Academic Press.

Rustambekovich, Y. N., Abdujalilovich, J. O., & Og'Li, I. M. T. L. (2019). IMPROVEMENT MEASUREMENTS OF ELECTROMAGNETIC FLOW METERS. *European science review*(5-6).

Salort, J., Rusaouën, É., Robert, L., Du Puits, R., Loesch, A., Pirotte, O., . . . Chillà, F. (2018). A local sensor for joint temperature and velocity measurements in turbulent flows. *Review of Scientific Instruments, 89*(1), 015005.

Schena, E., Massaroni, C., Saccomandi, P., & Cecchini, S. (2015). Flow measurement in mechanical ventilation: A review. *Medical engineering & physics, 37*(3), 257-264.

Sepúlveda, A., Fachin, F., de Villoria, R. G., Wardle, B., Viana, J., Pontes, A., & Rocha, L. A. (2011). Nanocomposite flexible pressure sensor for biomedical applications. *Procedia Engineering, 25*, 140-143.

Shakir, A., Srihari, K., Murcko, B., Yun, C., & Sulouff, B. (2008). *Flow sensor using micromachined pressure sensor*. Paper presented at the SENSORS, 2008 IEEE.

Shang, X., Huang, X., & Yang, C. (2016). Vortex generation and control in a microfluidic chamber with actuations. *Physics of Fluids, 28*(12), 122001.

Shercliff, J. A. (1962). *The theory of electromagnetic flow-measurement*: CUP Archive.

Siddiqui, A., Haroon, T., Mirza, A., & Ansari, A. (2013). Steady non isothermal two-dimensional flow of Newtonian fluid in a stenosed channel. *Theory and Applications of Mathematics & Computer Science, 3*(2), 75–92-75–92.

Silva, G., Semiao, V., & Reis, N. (2019). Rotating microchannel flow velocity measurements using the stationary micro-PIV technique with application to lab-on-a-CD devices. *Flow Measurement and Instrumentation, 67*, 153-165.

SmartMeasurement™. (2020). from https://www.smartmeasurement.com/positive-displacement-measuring-principle/

Smith, R., Sparks, D. R., Riley, D., & Najafi, N. (2008). A MEMS-based Coriolis mass flow sensor for industrial applications. *IEEE Transactions on Industrial Electronics, 56*(4), 1066-1071.

Sparreboom, W., Van de Geest, J., Katerberg, M., Postma, F., Haneveld, J., Groenesteijn, J., . . . Lötters, J. (2013). Compact mass flow meter based on a micro Coriolis flow sensor. *Micromachines, 4*(1), 22-33.

Stern, L., Bakal, A., Tzur, M., Veinguer, M., Mazurski, N., Cohen, N., & Levy, U. (2014). Doppler-based flow rate sensing in microfluidic channels. *Sensors, 14*(9), 16799-16807.

Suda, M., Onoguchi, M., Tomiyama, T., Ishihara, K., Takahashi, N., Sakurai, M., . . . Kumita, S.-i. (2016). The reproducibility of time-of-flight PET and conventional PET for the quantification of myocardial blood flow and coronary flow reserve with 13 N-ammonia. *Journal of Nuclear Cardiology, 23*(3), 457-472.

Thanh-Vinh, N., Matsumoto, K., & Shimoyama, I. (2015). *A viscometer based on vibration of droplets on a piezoresistive cantilever array.* Paper presented at the 2015 28th IEEE International Conference on Micro Electro Mechanical Systems (MEMS).

Toda, M., Inomata, N., Ono, T., & Voiculescu, I. (2017). Cantilever beam temperature sensors for biological applications. *IEEJ Transactions on Electrical and Electronic Engineering, 12*(2), 153-160.

Tovar-Lopez, F., Thurgood, P., Gilliam, C., Nguyen, N., Pirogova, E., Khoshmanesh, K., & Baratchi, S. (2019). A microfluidic system for studying the effects of disturbed flow on endothelial cells. *Frontiers in bioengineering and biotechnology, 7*, 81.

Travagliati, M., Girardo, S., Pisignano, D., Beltram, F., & Cecchini, M. (2013). Easy monitoring of velocity fields in microfluidic devices using spatiotemporal image correlation spectroscopy. *Analytical chemistry, 85*(17), 8080-8084.

Tung, S., Kim, J.-W., Malshe, A., Lee, C., & Pooran, R. (2003). *A cellular motor driven microfluidic system.* Paper presented at the TRANSDUCERS'03. 12th International Conference on Solid-State Sensors, Actuators and Microsystems. Digest of Technical Papers (Cat. No. 03TH8664).

Van Kuijk, J., Lammerink, T., De Bree, H.-E., Elwenspoek, M., & Fluitman, J. (1995). Multi-parameter detection in fluid flows. *Sensors and actuators A: Physical, 47*(1-3), 369-372.

Vögtli, M. (2011). *Nanomechanical detection of drug-target interactions using cantilever sensors.* UCL (University College London).

Walther, M., Fleming, P. M., Padovani, F., & Hegner, M. (2015). An optimized measurement chamber for cantilever array measurements in liquid incorporating an automated sample handling system. *EPJ Techniques and Instrumentation, 2*(1), 1-24.

Wang, T., & Baker, R. (2014). Coriolis flowmeters: a review of developments over the past 20 years, and an assessment of the state of the art and likely future directions. *Flow Measurement and Instrumentation, 40*, 99-123.

Wang, Y.-H., Chen, C.-P., Chang, C.-M., Lin, C.-P., Lin, C.-H., Fu, L.-M., & Lee, C.-Y. (2009). MEMS-based gas flow sensors. *Microfluidics and nanofluidics, 6*(3), 333.

Whitesides, G. M. (2006). The origins and the future of microfluidics. *Nature, 442*(7101), 368-373.

Yang, G., Pang, G., Pang, Z., Gu, Y., Mäntysalo, M., & Yang, H. (2018). Non-invasive flexible and stretchable wearable sensors with nano-based enhancement for chronic disease care. *IEEE reviews in biomedical engineering, 12*, 34-71.

Yogeswaran, N., Tinku, S., Khan, S., Lorenzelli, L., Vinciguerra, V., & Dahiya, R. (2015). *Stretchable resistive pressure sensor based on CNT-PDMS nanocomposites.* Paper presented at the 2015 11th Conference on Ph. D. Research in Microelectronics and Electronics (PRIME).

Yoon, S. G., & Chang, S. T. (2017). Microfluidic capacitive sensors with ionic liquid electrodes and CNT/PDMS nanocomposites for simultaneous sensing of pressure and temperature. *Journal of Materials Chemistry C, 5*(8), 1910-1919.

Yunus, A. C. (2010). Fluid Mechanics: Fundamentals And Applications (Si Units): Tata McGraw Hill Education Private Limited.

Zarifi, M. H., Sadabadi, H., Hejazi, S. H., Daneshmand, M., & Sanati-Nezhad, A. (2018). Noncontact and nonintrusive microwave-microfluidic flow sensor for energy and biomedical engineering. *Scientific reports, 8*(1), 1-10.

Zhang, H., Guo, C., & Lin, J. (2019). Effects of velocity profiles on measuring accuracy of transit-time ultrasonic flowmeter. *Applied Sciences, 9*(8), 1648.

Zheng, D., Zhang, T., & Hu, Y. (2007). Experimental investigations of the location of a piezoelectric probe in a vortex flow sensor. *Measurement Science and Technology, 18*(12), 3777.

Zhou, G., Wang, Y., & Cui, L. (2015). Biomedical sensor, device and measurement systems. *Advances in Bioengineering, 177*.

APPENDICES

APPENDIX A:
SENSOR CHARACTERIZATION

Figure A1

Setup for Change in Resistance with Respect to Bending in the MWCNT-PDMS Film

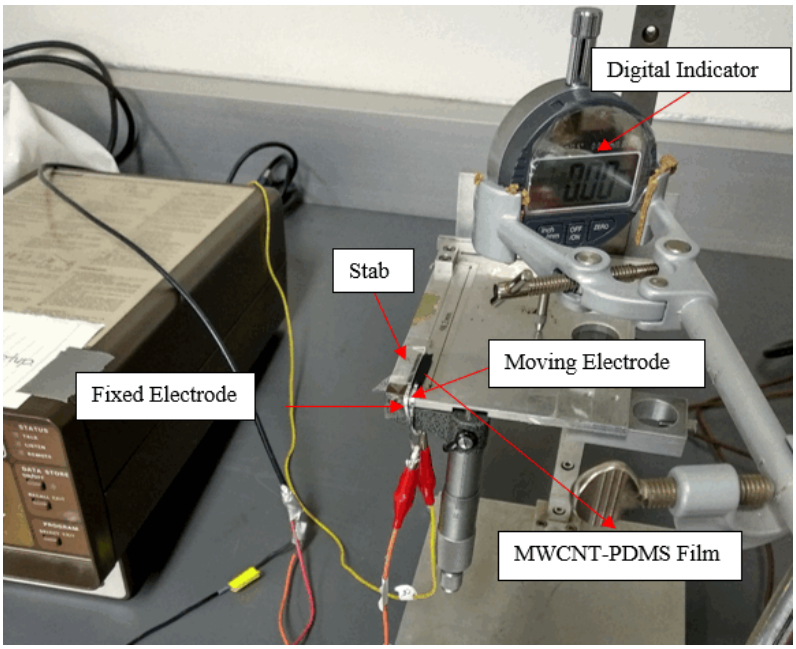

Figure A2

An overview of Elastic Modulus for Different CNT-PDMS Films

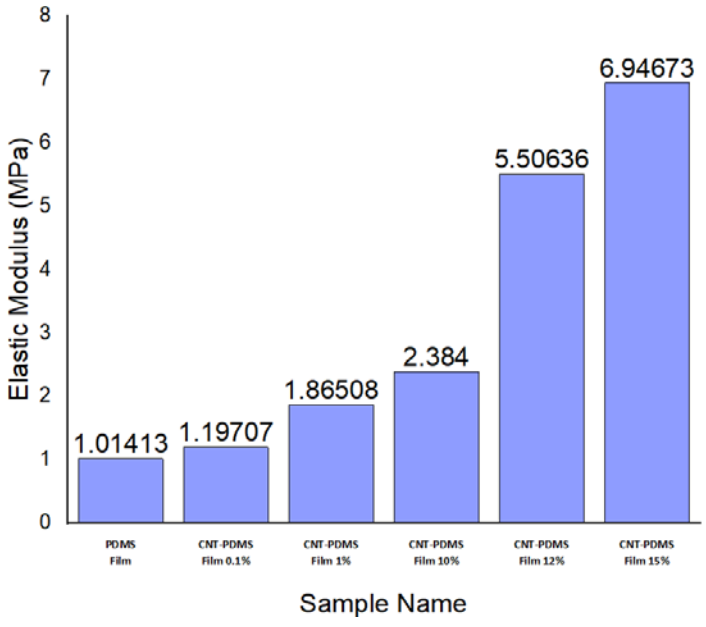

Figure A3

An overview of Average Contact Angle for Different CNT-PDMS Films

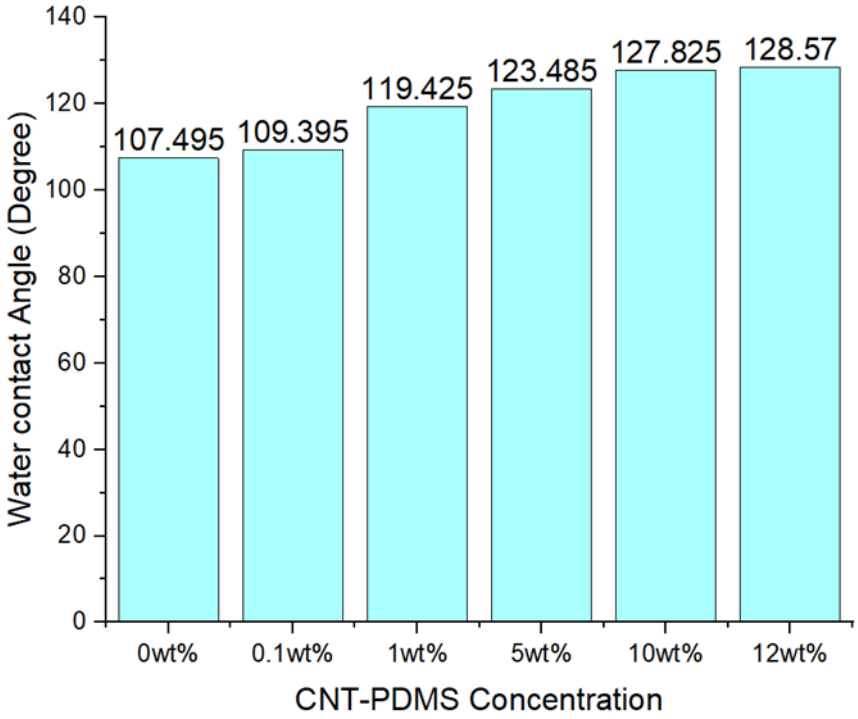

APPENDIX B:
SYSTEM PERFORMANCE

Figure B1: Change in Resistance for Different Flow Rates for Individual Observation

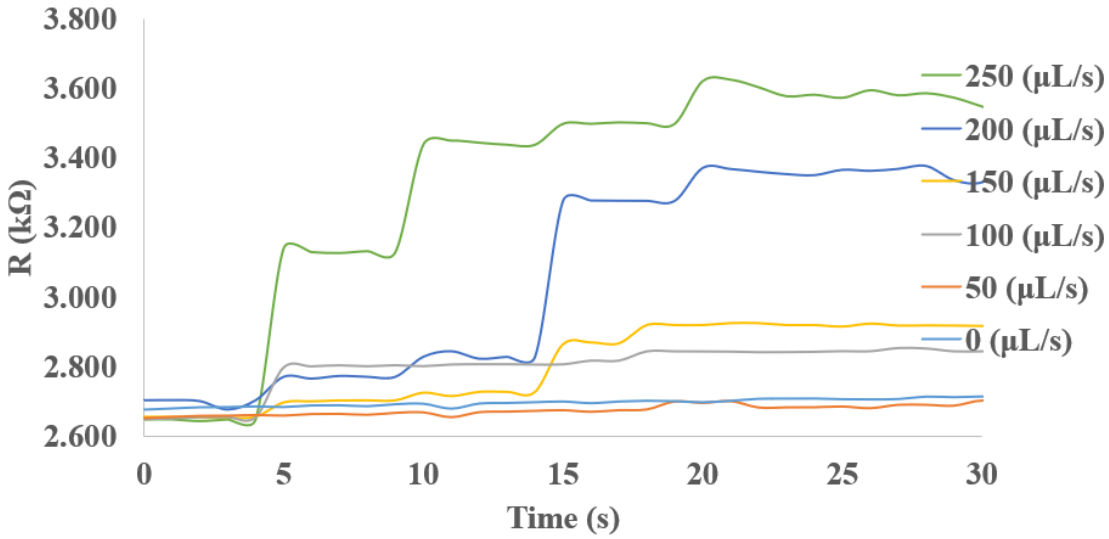

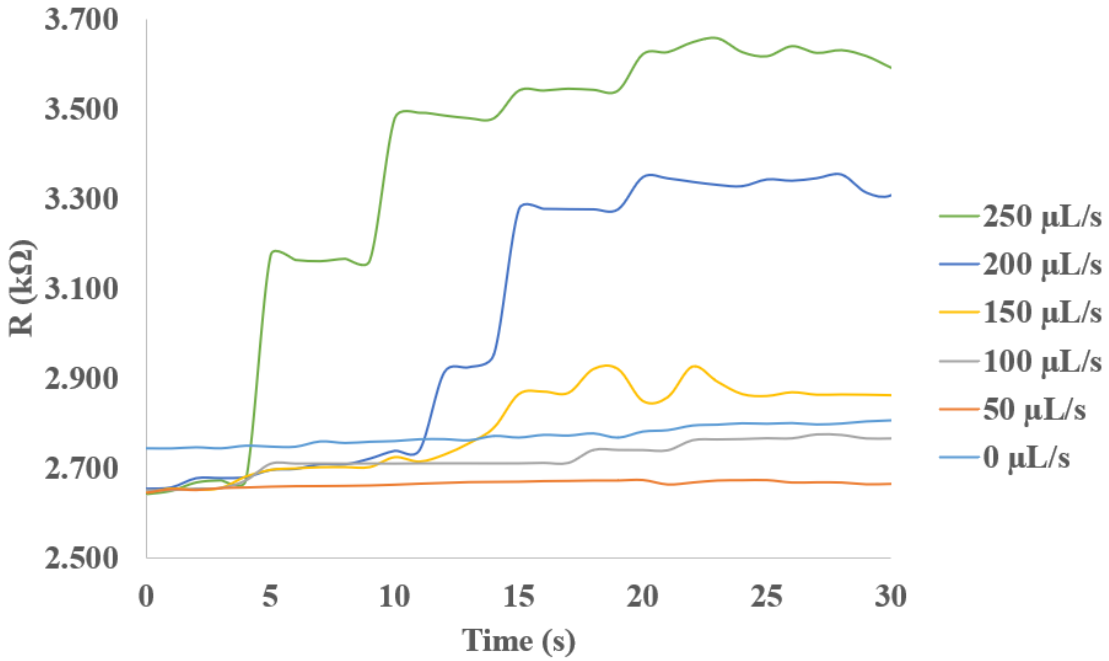

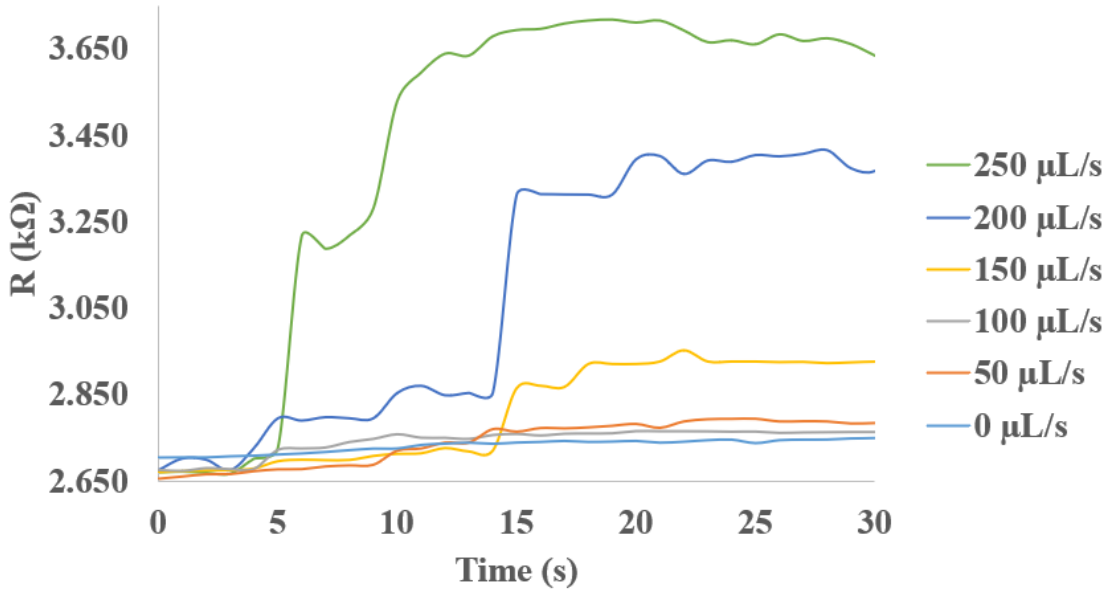
3.650
3.450
3.250
3.050
2.850
2.650
R (kΩ)
0
5
10
15
20
25
30
Time (s)
250 µL/s
200 µL/s
150 µL/s
100 µL/s
50 µL/s
0 µL/s

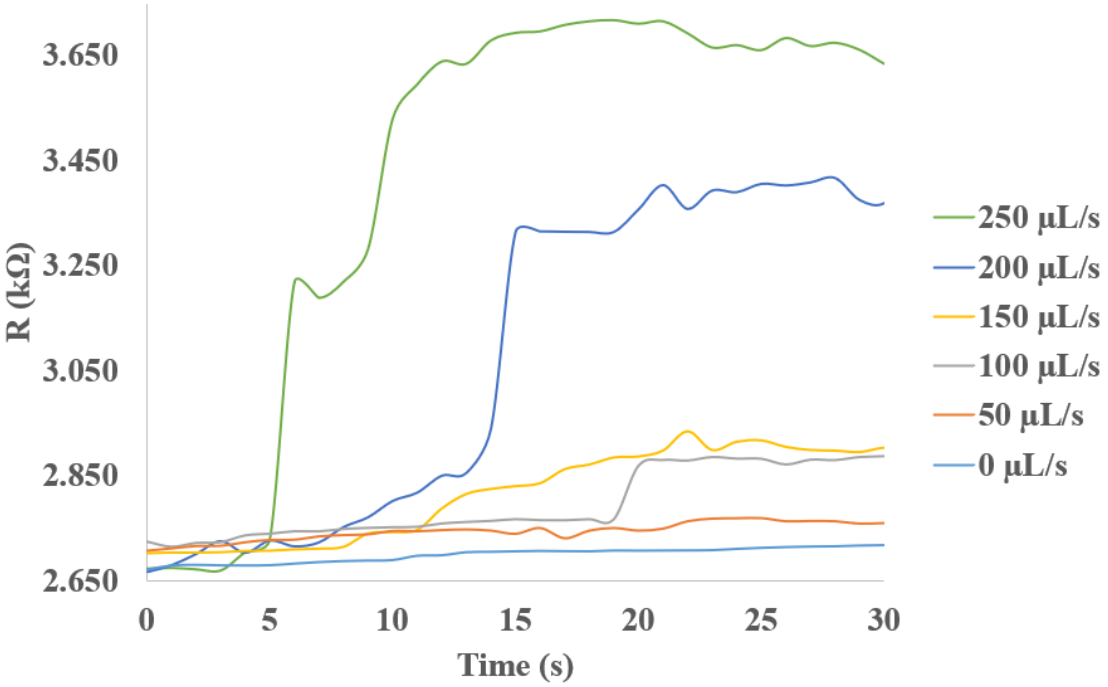
3.650
3.450
3.250
3.050
2.850
2.650
R (kΩ)
0
5
10
15
20
25
30
Time (s)
250 µL/s
200 µL/s
150 µL/s
100 µL/s
50 µL/s
0 µL/s

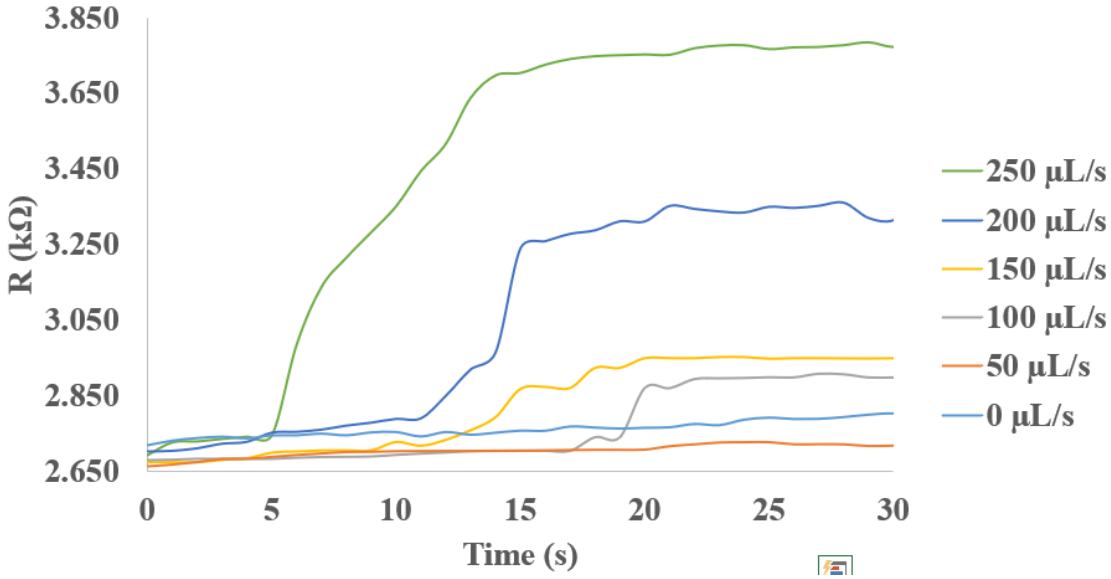
3.850
3.650
3.450
3.250
3.050
2.850
2.650
R (kΩ)
0
5
10
15
20
25
30
Time (s)
250 µL/s
200 µL/s
150 µL/s
100 µL/s
50 µL/s
0 µL/s

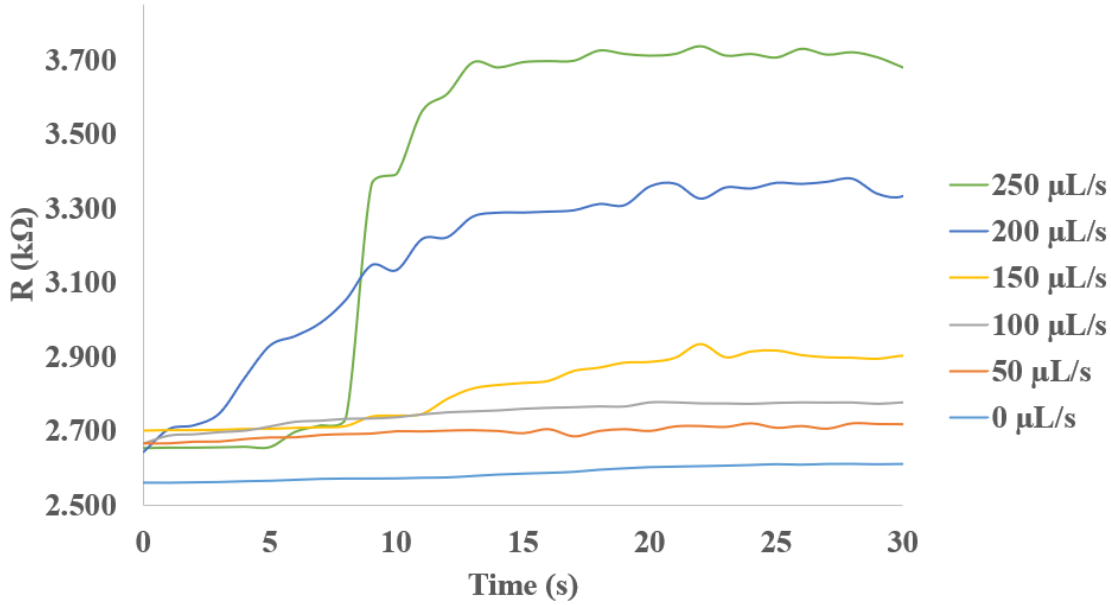
3.700
3.500
3.300
3.100
2.900
2.700
2.500
R (kΩ)
0
5
10
15
20
25
30
Time (s)
250 µL/s
200 µL/s
150 µL/s
100 µL/s
50 µL/s
0 µL/s